The Spatio-Temporal Control of Zygotic Genome Activation

George E. Gentsch,[1,*] Nick D. L. Owens,[2] and James C. Smith[1,3,*]

[1]Developmental Biology Laboratory, Francis Crick Institute, London, NW1 1AT, UK
[2]Department of Stem Cell and Developmental Biology, Pasteur Institute, 75015 Paris, France
[3]Lead Contact
*Correspondence: george.gentsch@crick.ac.uk (G.E.G.) and jim.smith@crick.ac.uk (J.C.S.)

SUMMARY

One of the earliest and most significant events in embryonic development is zygotic genome activation (ZGA). In several species, bulk transcription begins at the mid-blastula transition (MBT) when, after a certain number of cleavages, the embryo attains a particular nuclear-to-cytoplasmic (N/C) ratio, maternal repressors become sufficiently diluted, and the cell cycle slows down. Here we resolve the frog ZGA in time and space by profiling RNA polymerase II (RNAPII) engagement and its transcriptional readout. We detect a gradual increase in both the quantity and the length of RNAPII elongation before the MBT, revealing that >1,000 zygotic genes disregard the N/C timer for their activation, and that the sizes of newly transcribed genes are not necessarily constrained by cell cycle duration. We also find that Wnt, Nodal and BMP signaling together generate most of the spatio-temporal dynamics of regional ZGA, directing the formation of orthogonal body axes and proportionate germ layers.

INTRODUCTION

The genomes of multicellular organisms are transcriptionally silent at the time of fertilisation, and the events of early development, including zygotic (also known as embryonic) genome activation (ZGA), are directed by maternal gene products (De Iaco et al., 2019; Eckersley-Maslin et al., 2019; Gentsch et al., 2018b; Lee et al., 2013; Leichsenring et al., 2013; Liang et al., 2008). The number of cell cycles after which ZGA becomes essential for development (at which embryos arrest if transcription is inhibited) is highly reproducible within each species. In the zebrafish, the frog *Xenopus* and the fruit fly *Drosophila*, this occurs after 10, 12 and 13 cell cycles, respectively, at the so-called mid-blastula transition (MBT) (Blythe and Wieschaus, 2015; Gentsch et al., 2018b; Kane and Kimmel, 1993; Newport and Kirschner, 1982a). Early development in these species occurs with no gain in cytoplasmic volume, and studies in *Xenopus* suggest that ZGA is triggered at a particular nuclear-to-cytoplasmic (N/C) ratio, when the increasing amount of nuclear DNA titrates out maternally deposited repressors (Newport

33 and Kirschner, 1982b). Slower-developing mammalian embryos show major waves of RNA
34 polymerase II (RNAPII)-mediated transcription as early as the 2-cell stage in mice (Bolton et
35 al., 1984; Hamatani et al., 2004) and 4- to 8-cell stage in humans (Braude et al., 1988; Vanessa
36 et al., 2011). This occurs days before the formation of the blastocyst, which, like the blastula,
37 contains the pluripotent cells that form the embryo proper.

38 In *Xenopus*, ZGA is associated with changes in cell behaviour after the MBT. First, rapid and
39 nearly synchronous cell cleavages give way to longer and asynchronous cell divisions
40 (Anderson et al., 2017; Newport and Kirschner, 1982a). Second, embryonic cells acquire the
41 ability to respond to inductive signaling (Gentsch et al., 2018b), causing them to become motile,
42 to establish dorso-ventral patterning, and to contribute to one or two of the three germ layers
43 (endoderm, mesoderm and ectoderm). These germ layers emerge first during gastrulation and
44 are the primordia of all organs. Third, embryos show accelerated degradation of maternal RNA,
45 and fourth, cells gain apoptotic (Stack and Newport, 1997) and immunogenic (Gentsch et al.,
46 2018a) capabilities.

47 While large-scale ZGA occurs at the MBT, some genes escape the repressive environment of
48 the early embryo, and nascent transcripts can be detected in *Xenopus* during rapid cleavage
49 stages. For example, primary microRNA transcripts of the polycistronic MIR-427 gene (Lund et
50 al., 2009) are detectable in *X. tropicalis* after just three cell divisions (Owens et al., 2016). MIR-
51 427, like its zebrafish equivalent MIR-430, is activated at early stages by the synergistic and
52 pioneering activities of maternal members of the SoxB1 and Pou5F (Oct4) transcription factor
53 (TF) families (Gentsch et al., 2018b; Heyn et al., 2014; Lee et al., 2013). These core
54 pluripotency TFs, represented by Sox3 and Pou5f3 in *Xenopus*, are characterized by ubiquitous
55 and high translation frequencies in pre-MBT embryos (Gentsch et al., 2018b; Lee et al., 2013).
56 Zygotic transcription of the Nodal-encoding genes *nodal3/5/6*, and of the homeobox genes
57 *siamois1/2*, is initiated by nuclear β-catenin as early as the 32-cell stage (Owens et al., 2016;
58 Skirkanich et al., 2011; Yang et al., 2002).

59 While miR-427 (and miR-430 in zebrafish) contributes to the clearance of maternal RNA
60 (Giraldez et al., 2006; Lund et al., 2009), *nodal* and *siamois* gene initiate the formation of the
61 germ layers and body axes (Agius et al., 2000; Lemaire et al., 1995). All these genes, and other
62 early-activated genes in *Drosophila*, *Xenopus* and zebrafish, have coding sequences of <1 kb
63 and either no introns or just a few (Heyn et al., 2014). It has been suggested that the early rapid
64 cell cycles cause DNA replication machinery to interfere with the transcription of larger genes
65 (Shermoen and O'Farrell, 1991), a suggestion supported, to date, by the profiling of nascent
66 transcripts (Heyn et al., 2014). We note, however, that the detection and temporal resolution of
67 de novo transcription can be particularly challenging for genes that have both maternal and
68 zygotic transcripts.

69 Here we use the continuous occupancy of RNAPII along gene bodies as a method to record
70 ZGA. In contrast to transcript profiling techniques, this method (1) directly determines the

activity of every gene; (2) is independent of metabolic labeling (Heyn et al., 2014) and of any gene feature such as introns (Lee et al., 2013), single nucleotide polymorphisms (Harvey et al., 2013; Lott et al., 2011) or transcript half-lives; and (3) circumvents difficulties in detecting nascent transcripts in a large pool of maternal transcripts. By combining these data with the profiling of the transcriptome along the primary body axes (Blitz et al., 2017), we resolve ZGA in time and space for wild-type and various loss-of-function embryos. We provide evidence that runs counter to our original understanding of the cell cycle or of the N/C ratio in constraining gene expression before MBT. And finally, we show how signaling initiates and coordinates spatio-temporal ZGA in the *Xenopus* embryo.

RESULTS

RNAPII Profiling Reveals Exponential ZGA before MBT

In an effort to resolve the progression of ZGA, we profiled chromatin for RNAPII engagement on hand-sorted *X. tropicalis* embryos over six developmental stages from the 32-cell to the late gastrula stage (Figure 1A,B). RNAPII was localized on the genome by chromatin immunoprecipitation followed by deep sequencing (ChIP-Seq). We complemented RNAPII profiling with high time-resolution transcriptomics (Owens et al., 2016) counting both exonic and intronic RNA at 30-min intervals from fertilization to the late gastrula stage (Figures 1A,B and S1A,B). For both maternal and zygotic genes, the detection threshold was set to ≥3 transcripts per million (TPM) averaged over any 1-h window during this developmental period to avoid genes with general low-level expression. This restricted the analysis to 13,042 genes (Figure 1B). These genes were considered active when we detected simultaneously RNAPII enrichment along their full length (see Transparent Methods) as well as the presence of the corresponding transcripts. In doing so, we used a low threshold of ≥0.1 TPM so as not to miss the onset of gene transcription. RNAPII-guided ZGA profiling was verified in part by active post-translational histone marks (Hontelez et al., 2015) and by differential expression methods aiming at detecting nascent transcripts. Thus, zygotic transcript depletion (by blocking RNAPII elongation with α-amanitin) (Gentsch et al., 2018b) or enrichment (by selecting 4-thiouridine [4sU] tagged transcripts at the MBT and the mid-gastrula stage) showed substantial overlaps and positive correlations with RNAPII-covered genes (Figures 1A,B and S1C,D and Tables S1 and S2).

This analysis revealed an exponential ZGA before the MBT with 27, 144 and 1,044 active genes after 5 (32-cell, ~2.5 hpf), 7 (128-cell, ~3 hpf) and 10 (1,024-cell, ~4 hpf) cell cycles, respectively. Gene activation reached its peak at the MBT (~4.5 hpf), with 1,854 newly-activated genes, before dropping to 724 genes at the early-to-mid gastrula stage (~7.5 hpf) and increasing again to 1,214 genes towards the end of gastrulation (~10 hpf) (Figures 1B,C and S1E and Table S2). The dramatic increase in transcriptional activity that occurs in the 1.5 hours between the 128-cell stage and the MBT can be illustrated by Hilbert curves (Figure 1C), which

108 provide a genome-wide overview of RNAPII enrichment by folding chromosomes into two-
109 dimensional space-filling and position-preserving plots (Gu et al., 2016). While most zygotic
110 genes remain active beyond the mid-gastrula stage, 197 (including *siamois2* [*sia2*], *nodal5* and
111 *znf470*) of the 4,836 zygotic genes (~4%) are deactivated within ~6 h of development (Figures
112 1C and S1F,G). Slightly less than one third of the activated genes were differentially expressed
113 along either or both of the animal-vegetal and dorso-ventral axes (Figures 1D and S1F).

114 The temporal order of enriched biological processes supported by ZGA matched the regulatory
115 flow of gene expression, starting with nucleosome assembly, nucleic acid synthesis, mRNA
116 metabolism and production, post-translational modification and degradation of proteins (Figure
117 1E). The earliest transcriptional engagement, beginning at the 32 to 128-cell stages, was
118 detected in gene clusters of tens to hundreds of kilobases (Figures 1A,C and S1H-J). These
119 clusters featured close relatives of the same genes, some of which are critical to Nodal signaling
120 (Nodal ligands), the formation of the Spemann organiser (Siamois homeobox transcription
121 factors), nucleosome assembly (histones), mRNA decay (MIR-427), and ongoing gene
122 regulation (zinc finger [ZF] transcription factors with on average 10 Cys2-His2 [C2H2] domains;
123 Figure S1J). These earliest activated genes were shorter and encoded smaller proteins than
124 those within the maternal pool or those that are activated post-MBT (Figures 1F and S1K). The
125 non-coding features that contributed most to the differences in length were the 3' UTRs and
126 introns (Figure S1K).

127 We noted that the shorter zygotic genes observed before the MBT did not correlate strictly with
128 the time constraints imposed by short cell cycles. We detected increasing and wider spread of
129 de novo recruitment of RNAPII before the MBT, when cleavages continue to occur at rapid and
130 near-constant pace (Figures 1F and S1K). During this period, the median length of activated
131 genes (and their coding sequences) increases from ~0.9 kb (~0.4 kb) to ~5.9 kb (~0.9 kb).
132 However, it was not until after the MBT that the overall architecture of zygotic and maternal
133 genes became indistinguishable (Figures 1F and S1K). Temporal comparison of RNAPII
134 engagement and total RNA profiling suggested that the zygotic contribution to the transcriptome
135 (as calculated by the number of zygotic genes divided by the number of genes with ≥0.1 TPM
136 maternal transcripts averaged over the first hour post-fertilisation when the entire zygotic
137 genome is still transcriptionally inactive) rose within seven cell cycles from ~0.2% at the 32-cell
138 stage to ~22% at the MBT (Figure 1G). Further maternal degradation and more moderate
139 transcriptional engagement extended the zygotic contribution to about one third of the
140 transcriptome by the late gastrula stage. Maternal transcripts (≥0.1 TPM, see above) were
141 detected for ~67% of newly activated genes (18 out of 27 genes) at the 32-cell stage, ~85%
142 (99/117) at the 128-cell stage, ~87% (780/900) at the 1,024-cell stage, ~95% (1,754/1,854) at
143 the MBT, ~89% (644/724) at the mid-gastrula stage and ~90% (1,094/1,214) at the late gastrula
144 stage (Table S2). Altogether ~91% (4,389/4,836) of newly activated genes have ≥0.1 TPM
145 maternal contribution.

146 **Wnt, Nodal and BMP Signals Are Key Drivers of Regional ZGA**

147 We next sought to investigate the single and combined effects of different inductive signals on
148 the spatio-temporal dynamics of ZGA. The early vertebrate embryo employs canonical Wnt,
149 Nodal and BMP signals and their key transcriptional effectors β-catenin, Smad2 and Smad1,
150 respectively, to establish the primary body axes and the three germ layers (reviewed by Arnold
151 and Robertson, 2009 and Kimelman, 2006). In *Xenopus*, β-catenin first translocates to the
152 nuclei of dorsal blastomeres at the 32-cell stage (Larabell et al., 1997; Schneider et al., 1996)
153 (Figure 2A). After the MBT, zygotic Wnt8a causes more nuclear β-catenin to accumulate around
154 the forming blastopore lip (Christian and Moon, 1993; Schohl and Fagotto, 2002). The nuclear
155 translocation of Smad1 and Smad2 is triggered around the MBT by various BMP and Nodal
156 ligands. Nuclear Smad1 is primarily detected on the ventral side and the blastocoel roof of the
157 embryo while nuclear Smad2 is detected within the vegetal hemisphere (VH) and the marginal
158 zone (MZ) (Faure et al., 2000; Schohl and Fagotto, 2002) (Figure 2A).

159 In an effort to inhibit canonical Wnt signaling, we injected into the *X. tropicalis* zygote a
160 previously validated antisense morpholino oligonucleotide (MO) which interferes with β-catenin
161 protein synthesis by annealing to the translation start codon (Heasman et al., 2000). Nodal and
162 BMP signals were selectively blocked by incubating dejellied embryos from the 8-cell stage in
163 the cell-permeable inhibitors SB431542 (Ho et al., 2006; Inman et al., 2002) and LDN193189
164 (Cuny et al., 2008; Young et al., 2017), respectively. The morphological phenotypes of these
165 single loss-of-function (LOF) treatments were consistent with previous observations and ranged
166 from impaired axial elongation causing the loss of tail structures (BMP, Reversade et al., 2005)
167 to severe gastrulation defects (Wnt, Heasman et al., 2000, and Nodal, Ho et al., 2006) as shown
168 in Figure 2B. Briefly, Nodal LOF impaired blastopore lip formation and bulk tissue movements
169 of gastrulation (bullet points in Figure 2B). However, it did not preclude subsequent elongation
170 of the antero-posterior axis. By contrast, Wnt LOF embryos underwent gastrulation (albeit
171 delayed and more circumferentially rather than in a dorsal to ventral wave), but failed to form
172 an antero-posterior axis, with both head and tail being absent. With respect to the joint effects
173 of Wnt, Nodal and BMP signaling, most dual and triple LOFs combined their individual
174 morphological defects such that, for example, Wnt/Nodal LOF resulted in the complete loss of
175 gastrulation and axial elongation. By contrast, Wnt/BMP LOF produced defects such as non-
176 fusing neural folds (arrowheads in Figure 2B), structures that were either absent in Wnt LOF
177 embryos or normal in BMP LOF embryos.

178 Changes to ZGA caused by the single or combined LOF of Wnt, Nodal and/or BMP were then
179 determined at the late blastula stage on a transcriptome-wide scale using deep RNA
180 sequencing (RNA-Seq). Analysis was limited to the 3,315 zygotic genes for which spatio-
181 temporal expression data is available (Blitz et al., 2017; Owens et al., 2016) and where reduced
182 expression (≥50% loss of exonic and/or intronic transcript counts, FDR ≤10%) could be
183 detected in α-amanitin-injected embryos (Figure 2C and Table S3) (Gentsch et al., 2018b). α-
184 Amanitin-mediated inhibition of RNAPII elongation impedes the morphogenetic tissue

185 movements of gastrulation and ultimately leads to early embryonic death (Gentsch et al.,
186 2018b). Spatial gene expression patterns were inferred from experiments comparing the
187 transcriptomes of embryos dissected along their animal-vegetal and dorso-ventral axes (Blitz
188 et al., 2017); we did not include the left-right axis because there were no significant differences
189 in gene expression across this axis at the gastrula stage (Blitz et al., 2017). The signal-mediated
190 transcriptional effects (1.5-fold change from control RNA level) on zygotic genes, 86%
191 (2840/3315) of which have ≥0.1 TPM maternal contribution, ranged from ~1.5% (~1.3% down
192 and ~0.2% up) to ~26% (~19% down and 7% up) for single BMP LOF and triple Wnt/Nodal/BMP
193 LOFs, respectively (Figure 2C). As expected, the transcript levels of genes whose expression
194 is solely zygotic were more strongly affected than those of zygotic genes with maternally
195 contributed transcripts (Figures 2C and 4A). The extent of ZGA mis-regulation largely reflected
196 the severity of the resulting morphological phenotypes at the late gastrula and the mid-tailbud
197 stage (Figure 2B,C).

198 In comparison, the LOFs of critical maternal TFs like Pou5f3/Sox3 or VegT (Gentsch et al.,
199 2018b) caused the mis-regulation of 61% (~24% down and ~37% up) and 13% (~6% down and
200 ~7% up) of zygotic genes, respectively. The LOFs of four zygotic T-box TFs (zVegT, Eomes,
201 Tbxt and Tbxt.2), all of which require Nodal signaling for their expression, caused slight mis-
202 regulation in 19% (~9% down and ~10% up) of the zygotic genes as detected over three
203 consecutive developmental time points during gastrulation (Table S3). Among the ZGA-
204 enriched biological functions (Figure 1D), Wnt, Nodal and BMP signals, like maternal
205 Pou5f3/Sox3 and VegT, strongly affected zygotic genes associated with cell migration,
206 gastrulation, dorso-ventral and antero-posterior body axis formation and regionalization (Figure
207 2D). Impaired tissue movements during gastrulation, as observed in various LOFs (Figure 2B
208 and Movie S1), was prefigured by a strong enrichment for cell migration-associated genes. The
209 genes suppressed or unaffected by the selected signals and maternal TFs were enriched for
210 the ZGA-critical biological processes of mRNA metabolism and translation. For instance, the
211 transient activation of the entire zinc finger cluster (Figure S2A) was not affected by any tested
212 LOF. Because family members are frequently cross-regulated, and the MBT-staged chromatin
213 contains many Krüppel-like zinc finger 'footprints' (Gentsch et al., 2018b), it is conceivable that
214 the unaffected, tissue-nonspecific part of ZGA is regulated by maternal zinc finger TFs. This
215 vertebrate gene regulatory branch may be more ancient than that of Pou5F/SoxB1 as zinc
216 finger TFs like Zelda are also key to ZGA of the invertebrate *Drosophila* (Liang et al., 2008).

217 Next, signal-dependent ZGA was resolved in time and space based on (i) the profiling of
218 RNAPII-engaged chromatin from the 32-cell stage to the MBT and (ii) known gene expression
219 patterns along the animal-vegetal and dorso-ventral axes (Blitz et al., 2017) (Figures 2E and
220 S2B-F). In line with the nuclear translocation of their signal mediators (Figure 2A), Wnt, Nodal
221 and BMP proved to be required for gene activation in different spatio-temporal domains of the
222 early embryo: β-catenin was needed for ~87% and ~46% of genes preferentially expressed on
223 the dorsal side and in the VH/MZ, respectively. Some of its target genes like *nodal3.1* and *sia2*

224 were already active by the 32-cell stage (Figures 1C and 2E). Upon Wnt LOF, the early
225 transcriptional down-regulation was followed by the mis-regulation of opposing cell fate
226 specifiers: the upregulation of ventral genes (e.g., *id2*, *szl*) and the downregulation of dorsal
227 genes (e.g., *chrd*, *otx2*). These observations suggest that β-catenin protects dorsal cells from
228 ventralization (Figures 2E and S2C).

229 Along similar lines, Nodal LOF embryos predominantly displayed a down-regulation of dorsal
230 (~63%) and VH/MZ-specific (~73%) genes, although there was no effect of Nodal LOF on the
231 earliest-activated genes at the 32-cell stage or on opposing cell fate regulators (Figure S2A,B).
232 Among the first genes to be sensitive to Nodal LOF was the MZ-specific FGF ligand *fgf20*,
233 activated by the 128-cell stage (Figures 1C and S2A,B). By contrast, BMP LOF caused a
234 decrease in ventrally-expressed gene expression (~45%) from the 1,024-cell stage onwards
235 (Figure S2A,C).

236 As a comparison, the ubiquitous expression of maternal Pou5f3/Sox3 was required for
237 transcription in all spatio-temporal domains, including, for example, the uniform expression of
238 miR-427 (Figure S2A,D). The requirement for Pou5f3/Sox3 was more marked, however, for
239 region-specific genes, in particular those expressed within animal- (~55%) and ventral-specific
240 (~67%) domains (Figure S2A,D). The maternal TF VegT promoted vegetal identity by activating
241 ~40% of genes transcriptionally enriched within its own expression domain, the vegetal
242 hemisphere, while suppressing genes that are expressed in the animal hemisphere like *foxi4.2*.
243 The requirement for VegT was similar in ventral- and dorsal-specific genes (~31% and ~30%
244 respectively).

245 **Wnt/BMP Synergy Enables Uniform ZGA Across the Dorso-Ventral Axis**

246 The relationships between inductive signals with respect to spatial aspects of ZGA was
247 explored by comparing zygotic transcriptomes in single and double LOF experiments.
248 Interestingly, while simultaneous loss of both Nodal and BMP function, or both Nodal and Wnt,
249 caused additive effects on gene expression compared to the single LOFs (Figures 3E and S3A-
250 N), simultaneous loss of both BMP and Wnt signaling showed a more synergistic effect (Figure
251 3A,F). These observations are consistent with the morphological consequences of single and
252 double LOFs (Figure 2B). Single LOF experiments revealed very little overlap between Wnt
253 and BMP gene targets (Figure 3B), a result consistent with their domains of activity which are,
254 initially, at opposite ends of the dorso-ventral axis. However, dual Wnt/BMP inhibition increased
255 the number of downregulated genes by 292, a rise of ~118% and ~664% with respect to
256 individual Wnt- and BMP-dependent genes respectively (Figure 3B). Interestingly, this synergy
257 affected 166 Nodal-dependent genes, most of which had uniform expression levels across the
258 dorso-ventral axis (Figure 3C,D,F-H). Thus, spatially-restricted Wnt, BMP and Nodal signals
259 act together to establish dorso-ventral expression uniformity of genes such as *tbxt* and *eomes*
260 (Figure 3I).
261

262 Overall, the loss of canonical Wnt, Nodal and/or BMP signaling caused the misregulation of
263 ~39% (~22.1% down, ~2.1% down/up and ~14.4% up) of genes activated at ZGA (Figure 4A).
264 These signals were required for most regional ZGA on the dorsal side (~89%) and in the VH
265 and MZ (~82%). Notably, their input affected virtually all genes (~98%, 56/57) with enriched
266 expression in the dorso-vegetal/MZ quadrant (Figure 4B,C). Thus, Wnt, Nodal and BMP
267 substantially contribute to regional ZGA in most anatomical domains of the early gastrula
268 embryo with the exception of animally enriched transcription (~19%). Animal- and ventral-
269 specific gene expression relies strongly on both activation by ubiquitous maternal TFs (e.g.
270 Pou5f3/Sox3) and on repression by signals (Figure 4B,D) and other maternal TFs (e.g. VegT)
271 on the opposite side (Figure S2F).

272 **DISCUSSION**

273 Our study provides two major insights into the mechanisms by which ZGA is initiated in time
274 and space in *Xenopus tropicalis*. The first concerns the temporal aspects, where we find that
275 RNAPII can be detected across gene bodies well before the MBT, during the period when rapid
276 synchronous cell divisions divide the zygote into 4,096 blastomeres (Figure 4E). The average
277 length of genes covered by RNAPII grows during this time, from ~1 kb at the 32-cell stage to
278 ~6 kb at the 1,024-cell stage; these figures compare with an average size of ~16 kb for
279 maternally-expressed genes and for genes expressed after the MBT. Recent long-read
280 sequencing of the zebrafish transcriptome at pre-MBT stages identified transcripts as long as
281 8 kb spanning multiple pri-miR-430 elements (Nudelman et al., 2018). Furthermore, RNAPII
282 elongation in pre-MBT *Drosophila* embryos occurred at rates of 2.4 to 3.0 kb/min (Chen et al.,
283 2013; Fukaya et al., 2017).

284 We do not know why RNAPII, despite its high abundance and its ability to promote rapid
285 elongation, is restricted at early stages from transcribing more genes and longer genes. It may,
286 perhaps, be a consequence of the gradual nature of the chromatin remodeling that occurs
287 during these stages, from the accessibility of *cis*-regulatory elements (Gentsch et al., 2018b;
288 Liu et al., 2018; Lu et al., 2016; Wu et al., 2016) to the spatial organisation of an initially
289 unstructured or highly variable chromatin landscape (Du et al., 2017; Flyamer et al., 2017; Hug
290 et al., 2017; Kaaij et al., 2018; Ke et al., 2017). Whatever the reason, the increase of elongated
291 RNAPII engagement between the 128-cell stage and the MBT indicates that a significant
292 component of ZGA disregards the N/C ratio which was originally thought to underlie the onset
293 of transcription at the MBT (Newport and Kirschner, 1982b). Similar conclusions have been
294 drawn from profiling the zygotic transcriptome of haploid *Drosophila* (Lu et al., 2009) and cell
295 cycle-arrested zebrafish (Chan et al., 2018). Thus, it is becoming clear from work in flies, fish
296 and frogs that ZGA starts before the MBT and accelerates thereafter (Ali-Murthy et al., 2013;
297 Collart et al., 2014; Mathavan et al., 2005; Owens et al., 2017; Tan et al., 2013), reaching a
298 peak at the MBT (reviewed by Jukam et al., 2017 and Langley et al., 2014).

299 These observations notwithstanding, it remains possible that cell cycles do contribute to the
300 temporal progression of ZGA and the exponential increase in the number of activated genes
301 before the MBT. In particular, cell cycles may accelerate chromatin remodeling by displacing
302 suppressors in mitotic chromatin and providing unique access to TFs (Halley-Stott et al., 2014)
303 and structural proteins of high-order chromatin (Ke et al., 2017). For example, maternal core
304 histones have been shown to prevent premature ZGA by competing with specific TFs (Joseph
305 et al., 2017).

306 In addition to the small sizes of the earliest activated genes, we observed that most of these
307 genes, which have no or few introns, code for groups of related factors like histones or zinc
308 finger TFs, and that they appear as clusters spanning up to several hundred kilobases. This is
309 in line with previous findings of the earliest active multicopy and intron-poor genes like miR-427
310 and *nodal5/6* in *Xenopus* embryos (Collart et al., 2014; Lund et al., 2009; Owens et al., 2016;
311 Skirkanich et al., 2011; Takahashi et al., 2006; Yanai et al., 2011; Yang et al. 2002) and miR-
312 430 in zebrafish and Medaka fish (Giraldez et al., 2005; Heyn et al., 2014; Tani et al., 2010).
313 The number and spatial proximity of clustered genes enhances transcriptional output by
314 allowing the sharing of multiple cis-regulatory elements (arranged as super-enhancers) (Whyte
315 et al., 2013) and by fortifying transcriptional condensates of TFs, coactivators and RNAPII
316 (Boija et al., 2018; Cho et al., 2018; Chong et al., 2018; Sabari et al., 2018; Shrinivas et al.,
317 2018). Overall, based on enriched gene functions, we discovered that ZGA exerts a temporal
318 control of gene expression from nucleosome remodeling before the MBT to protein degradation
319 after the MBT.

320 Our second insight concerns spatial ZGA, and the observation that we can assign a large
321 proportion of spatio-temporal ZGA to key signaling pathways (reviewed by Arnold and
322 Robertson, 2009 and Kimelman, 2006). Canonical Wnt, Nodal and BMP signaling govern
323 regional ZGA in line with the nuclear translocation of their signal mediators (Faure et al., 2000;
324 Larabell et al., 1997; Schohl and Fagotto, 2002). Thus, Nodal signaling predominantly affects
325 transcription within the vegetal hemisphere and marginal zone, while Wnt and BMP initiate
326 transcription in dorsal and ventral regions, respectively. The timing of regional ZGA is defined
327 by the sequential translocation of signal mediators such that nuclear β-catenin directs regional
328 ZGA at the 32-cell stage, followed by nuclear Smad2 at the 128-cell stage and Smad1 at the
329 1,024-cell stage. While Smad2-mediated signal transduction depends on the zygotic
330 transcription of its six Nodal ligands (Faure et al., 2000; Gentsch et al., 2018b; Jones et al.,
331 1995; Yang et al., 2002), canonical Wnt and BMP signaling are initiated by the maternally
332 inherited ligands Wnt11 and BMP2/4/7, respectively (Faure et al., 2000; Heasman, 2006; Tao
333 et al., 2005).

334 We also show that the synergy of opposing signals of the Wnt and BMP pathway affects many
335 Nodal-dependent genes with uniform expression along the dorso-ventral axis such as *eomes*
336 and *Brachyury* (*tbxt*). It is not yet clear whether Wnt/BMP synergy arises from joint chromatin

engagement or from mutual or post-translational interactions. For instance, Wnt8a signal can enhance BMP transcriptional readouts by inhibiting the phosphorylation of GSK3, which normally targets Smad1 for degradation (Fuentealba et al., 2007). However, the analysis of *Brachyury* gene regulation in zebrafish suggests that Wnt and BMP can be integrated at a single cis-regulatory DNA element and together with a separate Nodal-responsive DNA element they can establish uniform dorso-ventral expression (Harvey et al., 2010). This is further corroborated by our analysis of genome-wide chromatin engagement (Gentsch et al., 2018b): the canonical DNA recognition motif for the Wnt-associated basic helix-span-helix (bHSH) TF AP-2 was more enriched at Smad1 than Smad2 binding sites (Figure S3O).

We therefore propose that Wnt, BMP and Nodal signal mediators are critical to regional ZGA and that they balance initially opposing cell fate commitments. However, we have previously shown that signal integration also relies on maternal pioneer TFs like Pou5f3 and Sox3 to make signal-responsive *cis*-regulatory elements accessible for signal mediator binding. For example, Nodal-induced transcription of the *Brachyury* gene depends on the pioneering roles of maternal Pou5f3 and Sox3, and less on their transcriptional activities (Gentsch et al., 2018b).

Overall, we demonstrate that the temporal and spatial dynamics of regional ZGA are regulated by the sequential and spatially restricted translocation of Wnt, Nodal and BMP signal mediators. These events establish the formation of the primary body axes and germ layers of the embryo. Temporal RNAPII profiling indicates that >1,000 genes of increasing length are activated before MBT and that this substantial portion of ZGA is independent of both the classic N/C ratio and of cell cycle lengthening.

LIMITATIONS OF THE STUDY

We detected a dramatic increase in genome-wide recruitment of RNAPII over the cleavage stages during which the genome begins to be transcribed. We used within-sample normalization to scale developmental stage-specific RNAPII profiles. However, because of the large differences in total RNAPII enrichment between samples, chromatin spike-ins are now considered a more accurate method to normalize ChIP-Seq profiles across consecutive developmental stages (Chen et al., 2016). We combined separate whole-embryo determinations of RNAPII engagement and transcript levels to reveal the temporal dynamics of ZGA. This approach could be improved by profiling RNAPII-associated RNA to directly couple RNAPII elongation with transcript accumulation (e.g., Churchman and Weissman, 2011). In addition, the spatial resolution of ZGA, which is based on transcriptomics of dissected embryonic parts in our study, could be enhanced by various deep single-cell profiling and super-resolution imaging technologies. We show that most regional ZGA depends on Wnt, Nodal and BMP signals, but an important question remains: How are these signals integrated at the chromatin level to sustain RNAPII-mediated transcript elongation? In part, this could be

373 investigated by targeted genome editing to increase our understanding of signal-responsive
374 gene regulatory DNA.

375 ACKNOWLEDGEMENTS

376 We thank Abdul Sesay, Leena Bhaw, Harsha Jani, Deborah Jackson and Meena Anissi for
377 deep sequencing; Mareike Thompson for critical reading of the manuscript; and the Smith lab
378 for discussions and advice. G.E.G and J.C.S. were supported by the Medical Research Council
379 (program number U117597140) and are now supported by the Francis Crick Institute, which
380 receives its core funding from Cancer Research UK (FC001-157), the UK Medical Research
381 Council (FC001-157), and the Wellcome Trust (FC001-157).

382 AUTHOR CONTRIBUTIONS

383 Conceptualization, G.E.G.; Methodology, G.E.G.; Computational Code, G.E.G.; Formal
384 Analysis, G.E.G. and N.D.L.O.; Investigation, G.E.G.; Writing – Original Draft, G.E.G. and
385 J.C.S.; Writing – Review & Editing, G.E.G and J.C.S.; Funding Acquisition, J.C.S.

386 DECLARATION OF INTERESTS

387 The authors declare no competing interests.

388 REFERENCES

389 Agius, E., Oelgeschlager, M., Wessely, O., Kemp, C., and De Robertis, E.M. (2000).
390 Endodermal Nodal-related signals and mesoderm induction in Xenopus. Development *127*,
391 1173–1183.

392 Ali-Murthy, Z., Lott, S.E., Eisen, M.B., and Kornberg, T.B. (2013). An essential role for zygotic
393 expression in the pre-cellular Drosophila embryo. PLoS Genet. *9*, e1003428.

394 Anderson, G.A., Gelens, L., Baker, J.C., and Ferrell, J.E. (2017). Desynchronizing Embryonic
395 Cell Division Waves Reveals the Robustness of Xenopus laevis Development. Cell Rep. *21*,
396 37–46.

397 Arnold, S.J., and Robertson, E.J. (2009). Making a commitment: cell lineage allocation and
398 axis patterning in the early mouse embryo. Nat. Rev. Mol. Cell Biol. *10*, 91–103.

399 Boija, A., Klein, I.A., Sabari, B.R., Dall'Agnese, A., Coffey, E.L., Zamudio, A.V., Li, C.H.,
400 Shrinivas, K., Manteiga, J.C., Hannett, N.M., et al. (2018). Transcription Factors Activate
401 Genes through the Phase-Separation Capacity of Their Activation Domains. Cell *175*, 1842–
402 1855.e16.

403 Blitz, I.L., Paraiso, K.D., Patrushev, I., Chiu, W.T.Y., Cho, K.W.Y., and Gilchrist, M.J. (2017).
404 A catalog of Xenopus tropicalis transcription factors and their regional expression in the early
405 gastrula stage embryo. Dev. Biol. *426*, 409–417.

406 Blythe, S.A., and Wieschaus, E.F. (2015). Zygotic genome activation triggers the DNA
407 replication checkpoint at the midblastula transition. Cell *160*, 1169–1181.

408 Bolton, V.N., Oades, P.J., and Johnson, M.H. (1984). The relationship between cleavage,
409 DNA replication, and gene expression in the mouse 2-cell embryo. J. Embryol. Exp. Morph.
410 *79*, 139–163.

411 Braude, P., Bolton, V., and Moore, S. (1988). Human gene expression first occurs between
412 the four- and eight-cell stages of preimplantation development. Nature *332*, 459–461.

413 Chan, S.H., Tang, Y., Miao, L., Darwich-Codore, H., Vejnar, C.E., Beaudoin, J.-D., Musaev,
414 D., Fernandez, J.P., Moreno-Mateos, M.A., and Giraldez, A.J. (2018). Brd4 and P300
415 regulate zygotic genome activation through histone acetylation. bioRxiv 369231. DOI:
416 https://doi.org/10.1101/369231

417 Chen, K., Hu, Z., Xia, Z., Zhao, D., Li, W., and Tyler, J.K. (2015). The Overlooked Fact:
418 Fundamental Need for Spike-In Control for Virtually All Genome-Wide Analyses. Mol. Cell.
419 Biol. *36*, 662–667.

420 Chen, K., Johnston, J., Shao, W., Meier, S., Staber, C., and Zeitlinger, J. (2013). A global
421 change in RNA polymerase II pausing during the Drosophila midblastula transition. Elife *2*,
422 e00861.

423 Chiu, W.T., Le, R.C., Blitz, I.L., Fish, M.B., Li, Y., Biesinger, J., Xie, X., and Cho, K.W.Y.
424 (2014). Genome-wide view of TGFβ/Foxh1 regulation of the early mesendoderm program.
425 Development *141*, 1–114.

426 Cho, W.-K., Spille, J.-H., Hecht, M., Lee, C., Li, C., Grube, V., and Cisse, I.I. (2018). Mediator
427 and RNA polymerase II clusters associate in transcription-dependent condensates. Science
428 *361*, 412–415.

429 Chong, S., Dugast-Darzacq, C., Liu, Z., Dong, P., Dailey, G.M., Cattoglio, C., Heckert, A.,
430 Banala, S., Lavis, L., Darzacq, X., et al. (2018). Imaging dynamic and selective low-
431 complexity domain interactions that control gene transcription. Science *361*, eaar2555.

432 Christian, J.L., and Moon, R.T. (1993). Interactions between Xwnt-8 and Spemann organizer
433 signaling pathways generate dorsoventral pattern in the embryonic mesoderm of Xenopus.
434 Genes Dev. *7*, 13–28.

435 Collart, C., Owens, N.D.L., Bhaw-Rosun, L., Cooper, B., De Domenico, E., Patrushev, I.,
436 Sesay, A.K., Smith, J.N., Smith, J.C., and Gilchrist, M.J. (2014). High-resolution analysis of
437 gene activity during the Xenopus mid-blastula transition. Development *141*, 1927–1939.

438 Cuny, G.D., Yu, P.B., Laha, J.K., Xing, X., Liu, J.-F., Lai, C.S., Deng, D.Y., Sachidanandan,
439 C., Bloch, K.D., and Peterson, R.T. (2008). Structure-activity relationship study of bone
440 morphogenetic protein (BMP) signaling inhibitors. Bioorg. Med. Chem. Lett. *18*, 4388–4392.

441 De Iaco, A., Coudray, A., Duc, J., and Trono, D. (2019). DPPA2 and DPPA4 are necessary to
442 establish a 2C-like state in mouse embryonic stem cells. EMBO Reports e47382.

443 Du, Z., Zheng, H., Huang, B., Ma, R., Wu, J., Zhang, X., He, J., Xiang, Y., Wang, Q., Li, Y., et
444 al. (2017). Allelic reprogramming of 3D chromatin architecture during early mammalian
445 development. Nature *547*, 232–235.

446 Eckersley-Maslin, M., Alda-Catalinas, C., Blotenburg, M., Kreibich, E., Krueger, C., and Reik,
447 W. (2019). Dppa2 and Dppa4 directly regulate the Dux-driven zygotic transcriptional program.
448 Genes Dev. *33*, 194–208.

449 Faure, S., Lee, M.A., Keller, T., Dijke, ten, P., and Whitman, M. (2000). Endogenous patterns
450 of TGFbeta superfamily signaling during early Xenopus development. Development *127*,

451 2917–2931.

452 Flyamer, I.M., Gassler, J., Imakaev, M., Brandão, H.B., Ulianov, S.V., Abdennur, N., Razin,
453 S.V., Mirny, L.A., and Tachibana-Konwalski, K. (2017). Single-nucleus Hi-C reveals unique
454 chromatin reorganization at oocyte-to-zygote transition. Nature *544*, 110–114.

455 Fuentealba, L.C., Eivers, E., Ikeda, A., Hurtado, C., Kuroda, H., Pera, E.M., and De Robertis,
456 E.M. (2007). Integrating patterning signals: Wnt/GSK3 regulates the duration of the
457 BMP/Smad1 signal. Cell *131*, 980–993.

458 Fukaya, T., Lim, B., and Levine, M. (2017). Rapid Rates of Pol II Elongation in the Drosophila
459 Embryo. Curr. Biol. *27*, 1387–1391.

460 Gentsch, G.E., Spruce, T., Monteiro, R.S., Owens, N.D.L., Martin, S.R., and Smith, J.C.
461 (2018a). Innate Immune Response and Off-Target Mis-splicing Are Common Morpholino-
462 Induced Side Effects in Xenopus. Dev. Cell *44*, 597–610.e10.

463 Gentsch, G.E., Spruce, T., Owens, N.D.L., and Smith, J.C. (2018b). The role of maternal
464 pioneer factors in predefining first zygotic responses to inductive signals. bioRxiv 306803.
465 DOI: https://doi.org/10.1101/306803

466 Giraldez, A.J., Cinalli, R.M., Glasner, M.E., Enright, A.J., Thomson, J.M., Baskerville, S.,
467 Hammond, S.M., Bartel, D.P., and Schier, A.F. (2005). MicroRNAs regulate brain
468 morphogenesis in zebrafish. Science *308*, 833–838.

469 Giraldez, A.J., Mishima, Y., Rihel, J., Grocock, R.J., Van Dongen, S., Inoue, K., Enright, A.J.,
470 and Schier, A.F. (2006). Zebrafish MiR-430 promotes deadenylation and clearance of
471 maternal mRNAs. Science *312*, 75–79.

472 Gu, Z., Eils, R., and Schlesner, M. (2016). HilbertCurve: an R/Bioconductor package for high-
473 resolution visualization of genomic data. Bioinformatics *32*, 2372–2374.

474 Halley-Stott, R.P., Jullien, J., Pasque, V., and Gurdon, J. (2014). Mitosis gives a brief window
475 of opportunity for a change in gene transcription. PLoS Biol. *12*, e1001914.

476 Hamatani, T., Carter, M.G., Sharov, A.A., and Ko, M.S.H. (2004). Dynamics of global gene
477 expression changes during mouse preimplantation development. Dev. Cell *6*, 117–131.

478 Harvey, S.A., Sealy, I., Kettleborough, R., Fenyes, F., White, R., Stemple, D., and Smith, J.C.
479 (2013). Identification of the zebrafish maternal and paternal transcriptomes. Development
480 *140*, 2703–2710.

481 Harvey, S.A., Tümpel, S., Dubrulle, J., Schier, A.F., and Smith, J.C. (2010). no tail integrates
482 two modes of mesoderm induction. Development *137*, 1127–1135.

483 Heasman, J. (2006). Patterning the early Xenopus embryo. Development *133*, 1205–1217.

484 Heasman, J., Kofron, M., and Wylie, C. (2000). βCatenin Signaling Activity Dissected in the
485 Early Xenopus Embryo: A Novel Antisense Approach. Dev. Biol. *222*, 124–134.

486 Heyn, P., Kircher, M., Dahl, A., Kelso, J., Tomancak, P., Kalinka, A.T., and Neugebauer, K.M.
487 (2014). The earliest transcribed zygotic genes are short, newly evolved, and different across
488 species. Cell Rep. *6*, 285–292.

489 Ho, D.M., Chan, J., Bayliss, P., and Whitman, M. (2006). Inhibitor-resistant type I receptors
490 reveal specific requirements for TGF-beta signaling in vivo. Dev. Biol. *295*, 730–742.

491 Hontelez, S., van Kruijsbergen, I., Georgiou, G., van Heeringen, S.J., Bogdanović, O., Lister,
492 R., and Veenstra, G.J.C. (2015). Embryonic transcription is controlled by maternally defined

493 chromatin state. Nat. Commun. *6*, 10148.

494 Hug, C.B., Grimaldi, A.G., Kruse, K., and Vaquerizas, J.M. (2017). Chromatin Architecture
495 Emerges during Zygotic Genome Activation Independent of Transcription. Cell *169*, 216–
496 228.e219.

497 Inman, G.J., Nicolás, F.J., Callahan, J.F., Harling, J.D., Gaster, L.M., Reith, A.D., Laping,
498 N.J., and Hill, C.S. (2002). SB-431542 is a potent and specific inhibitor of transforming growth
499 factor-beta superfamily type I activin receptor-like kinase (ALK) receptors ALK4, ALK5, and
500 ALK7. Mol. Pharmacol. *62*, 65–74.

501 Jones, C.M., Kuehn, M.R., Hogan, B.L., Smith, J.C., and Wright, C.V. (1995). Nodal-related
502 signals induce axial mesoderm and dorsalize mesoderm during gastrulation. Development
503 *121*, 3651–3662.

504 Joseph, S.R., Pálfy, M., Hilbert, L., Kumar, M., Karschau, J., Zaburdaev, V., Shevchenko, A.,
505 and Vastenhouw, N.L. (2017). Competition between histone and transcription factor binding
506 regulates the onset of transcription in zebrafish embryos. Elife *6*, e23326.

507 Jukam, D., Shariati, S.A.M., and Skotheim, J.M. (2017). Zygotic Genome Activation in
508 Vertebrates. Dev. Cell *42*, 316–332.

509 Kaaij, L.J.T., van der Weide, R.H., Ketting, R.F., and de Wit, E. (2018). Systemic Loss and
510 Gain of Chromatin Architecture throughout Zebrafish Development. Cell Rep. *24*, 1–10.e4.

511 Kane, D.A., and Kimmel, C.B. (1993). The zebrafish midblastula transition. Development *119*,
512 447–456.

513 Ke, Y., Xu, Y., Chen, X., Feng, S., Liu, Z., Sun, Y., Yao, X., Li, F., Zhu, W., Gao, L., et al.
514 (2017). 3D Chromatin Structures of Mature Gametes and Structural Reprogramming during
515 Mammalian Embryogenesis. Cell *170*, 367–381.e20.

516 Kimelman, D. (2006). Mesoderm induction: from caps to chips. Nat. Rev. Genet. *7*, 360–372.

517 Langley, A.R., Smith, J.C., Stemple, D.L., and Harvey, S.A. (2014). New insights into the
518 maternal to zygotic transition. Development *141*, 3834–3841.

519 Larabell, C.A., Torres, M., Rowning, B.A., Yost, C., Miller, J.R., Wu, M., Kimelman, D., and
520 Moon, R.T. (1997). Establishment of the dorso-ventral axis in Xenopus embryos is presaged
521 by early asymmetries in beta-catenin that are modulated by the Wnt signaling pathway. J. Cell
522 Biol. *136*, 1123–1136.

523 Lemaire, P., Garrett, N., and Gurdon, J.B. (1995). Expression cloning of Siamois, a Xenopus
524 homeobox gene expressed in dorsal-vegetal cells of blastulae and able to induce a complete
525 secondary axis. Cell *81*, 85–94.

526 Lee, M.T., Bonneau, A.R., Takacs, C.M., Bazzini, A.A., Divito, K.R., Fleming, E.S., and
527 Giraldez, A.J. (2013). Nanog, Pou5f1 and SoxB1 activate zygotic gene expression during the
528 maternal-to-zygotic transition. Nature *503*, 360–364.

529 Leichsenring, M., Maes, J., Mössner, R., Driever, W., and Onichtchouk, D. (2013). Pou5f1
530 transcription factor controls zygotic gene activation in vertebrates. Science *341*, 1005–1009.

531 Liang, H.-L., Nien, C.-Y., Liu, H.-Y., Metzstein, M.M., Kirov, N., and Rushlow, C. (2008). The
532 zinc-finger protein Zelda is a key activator of the early zygotic genome in Drosophila. Nature
533 *456*, 400–403.

534 Liu, G., Wang, W., Hu, S., Wang, X., and Zhang, Y. (2018). Inherited DNA methylation primes
535 the establishment of accessible chromatin during genome activation. Genome Res. *28*, 998–
536 1007.

537 Lott, S.E., Villalta, J.E., Schroth, G.P., Luo, S., Tonkin, L.A., and Eisen, M.B. (2011).
538 Noncanonical compensation of zygotic X transcription in early Drosophila melanogaster
539 development revealed through single-embryo RNA-seq. PLoS Biol. *9*, e1000590.

540 Lu, F., Liu, Y., Inoue, A., Suzuki, T., Zhao, K., and Zhang, Y. (2016). Establishing Chromatin
541 Regulatory Landscape during Mouse Preimplantation Development. Cell *165*, 1375–1388.

542 Lu, X., Li, J.M., Elemento, O., Tavazoie, S., and Wieschaus, E.F. (2009). Coupling of zygotic
543 transcription to mitotic control at the Drosophila mid-blastula transition. Development *136*,
544 2101–2110.

545 Lund, E., Liu, M., Hartley, R.S., Sheets, M.D., and Dahlberg, J.E. (2009). Deadenylation of
546 maternal mRNAs mediated by miR-427 in Xenopus laevis embryos. RNA *15*, 2351–2363.

547 Mathavan, S., Lee, S.G.P., Mak, A., Miller, L.D., Murthy, K.R.K., Govindarajan, K.R., Tong,
548 Y., Wu, Y.L., Lam, S.H., Yang, H., et al. (2005). Transcriptome analysis of zebrafish
549 embryogenesis using microarrays. PLoS Genet. *1*, 260–276.

550 Newport, J., and Kirschner, M.W. (1982a). A major developmental transition in early xenopus
551 embryos: I. characterization and timing of cellular changes at the midblastula stage. Cell *30*,
552 675–686.

553 Newport, J., and Kirschner, M.W. (1982b). A major developmental transition in early xenopus
554 embryos: II. control of the onset of transcription. Cell *30*, 687–696.

555 Nudelman, G., Frasca, A., Kent, B., Sadler, K.C., Sealfon, S.C., Walsh, M.J., and Zaslavsky,
556 E. (2018). High resolution annotation of zebrafish transcriptome using long-read sequencing.
557 Genome Res. *28*, 1415-1425.

558 Owens, N.D.L., Blitz, I.L., Lane, M.A., Patrushev, I., Overton, J.D., Gilchrist, M.J., Cho,
559 K.W.Y., and Khokha, M.K. (2016). Measuring Absolute RNA Copy Numbers at High Temporal
560 Resolution Reveals Transcriptome Kinetics in Development. Cell Rep. *14*, 632–647.

561 Reversade, B., Kuroda, H., Lee, H., Mays, A., and De Robertis, E.M. (2005). Depletion of
562 Bmp2, Bmp4, Bmp7 and Spemann organizer signals induces massive brain formation in
563 Xenopus embryos. Development *132*, 3381–3392.

564 Sabari, B.R., Dall'Agnese, A., Boija, A., Klein, I.A., Coffey, E.L., Shrinivas, K., Abraham, B.J.,
565 Hannett, N.M., Zamudio, A.V., Manteiga, J.C., et al. (2018). Coactivator condensation at
566 super-enhancers links phase separation and gene control. Science *361*, eaar3958.

567 Schneider, S., Steinbeisser, H., Warga, R., and Hausen, P. (1996). Beta-catenin translocation
568 into nuclei demarcates the dorsalizing centers in frog and fish embryos. Mech. Dev. *57*, 191–
569 198.

570 Schohl, A., and Fagotto, F. (2002). Beta-catenin, MAPK and Smad signaling during early
571 Xenopus development. Development *129*, 37–52.

572 Shermoen, A.W., and O'Farrell, P.H. (1991). Progression of the cell cycle through mitosis
573 leads to abortion of nascent transcripts. Cell *67*, 303–310.

574 Shrinivas, K., Sabari, B.R., Coffey, E.L., Klein, I.A., Boija, A., Zamudio, A.V., Schuijers, J.,
575 Hannett, N.M., Sharp, P.A., Young, R.A., et al. (2018). Enhancer features that drive formation
576 of transcriptional condensates. bioRxiv 495606. DOI: https://doi.org/10.1101/495606

577 Skirkanich, J., Luxardi, G., Yang, J., Kodjabachian, L., and Klein, P.S. (2011). An essential
578 role for transcription before the MBT in Xenopus laevis. Dev. Biol. *357*, 478–491.

579 Stack, J.H., and Newport, J.W. (1997). Developmentally regulated activation of apoptosis
580 early in Xenopus gastrulation results in cyclin A degradation during interphase of the cell

581 cycle. Development *124*, 3185–3195.

582 Takahashi, S., Onuma, Y., Yokota, C., Westmoreland, J.J., Asashima, M., and Wright, C.V.E.
583 (2006). Nodal-related gene Xnr5 is amplified in the Xenopus genome. Genesis *44*, 309–321.

584 Tan, M.H., Au, K.F., Yablonovitch, A.L., Wills, A.E., Chuang, J., Baker, J.C., Wong, W.H., and
585 Li, J.B. (2013). RNA sequencing reveals a diverse and dynamic repertoire of the Xenopus
586 tropicalis transcriptome over development. Genome Res. *23*, 201–216.

587 Tani, S., Kusakabe, R., Naruse, K., Sakamoto, H., and Inoue, K. (2010). Genomic
588 organization and embryonic expression of miR-430 in medaka (Oryzias latipes): insights into
589 the post-transcriptional gene regulation in early development. Gene *449*, 41–49.

590 Tao, Q., Yokota, C., Puck, H., Kofron, M., Birsoy, B., Yan, D., Asashima, M., Wylie, C.C., Lin,
591 X., and Heasman, J. (2005). Maternal wnt11 activates the canonical wnt signaling pathway
592 required for axis formation in Xenopus embryos. Cell *120*, 857–871.

593 Vassena, R., Boué, S., González-Roca, E., Aran, B., Auer, H., Veiga, A., and Izpisúa
594 Belmonte, J.C. (2011). Waves of early transcriptional activation and pluripotency program
595 initiation during human preimplantation development. Development *138*, 3699–3709.

596 Whyte, W.A., Orlando, D.A., Hnisz, D., Abraham, B.J., Lin, C.Y., Kagey, M.H., Rahl, P.B.,
597 Lee, T.I., and Young, R.A. (2013). Master transcription factors and mediator establish super-
598 enhancers at key cell identity genes. Cell *153*, 307–319.

599 Wu, J., Huang, B., Chen, H., Yin, Q., Liu, Y., Xiang, Y., Zhang, B., Liu, B., Wang, Q., Xia, W.,
600 et al. (2016). The landscape of accessible chromatin in mammalian preimplantation embryos.
601 Nature *534*, 652–657.

602 Yanai, I., Peshkin, L., Jorgensen, P., and Kirschner, M.W. (2011). Mapping gene expression
603 in two Xenopus species: evolutionary constraints and developmental flexibility. Dev. Cell *20*,
604 483–496.

605 Yang, J., Tan, C., Darken, R.S., Wilson, P.A., and Klein, P.S. (2002). Beta-catenin/Tcf-
606 regulated transcription prior to the midblastula transition. Development *129*, 5743–5752.

607 Young, J.J., Kjolby, R.A.S., Wu, G., Wong, D., Hsu, S.-W., and Harland, R.M. (2017). Noggin
608 is required for first pharyngeal arch differentiation in the frog Xenopus tropicalis. Dev. Biol.
609 *426*, 245–254.

610 **MAIN FIGURES**

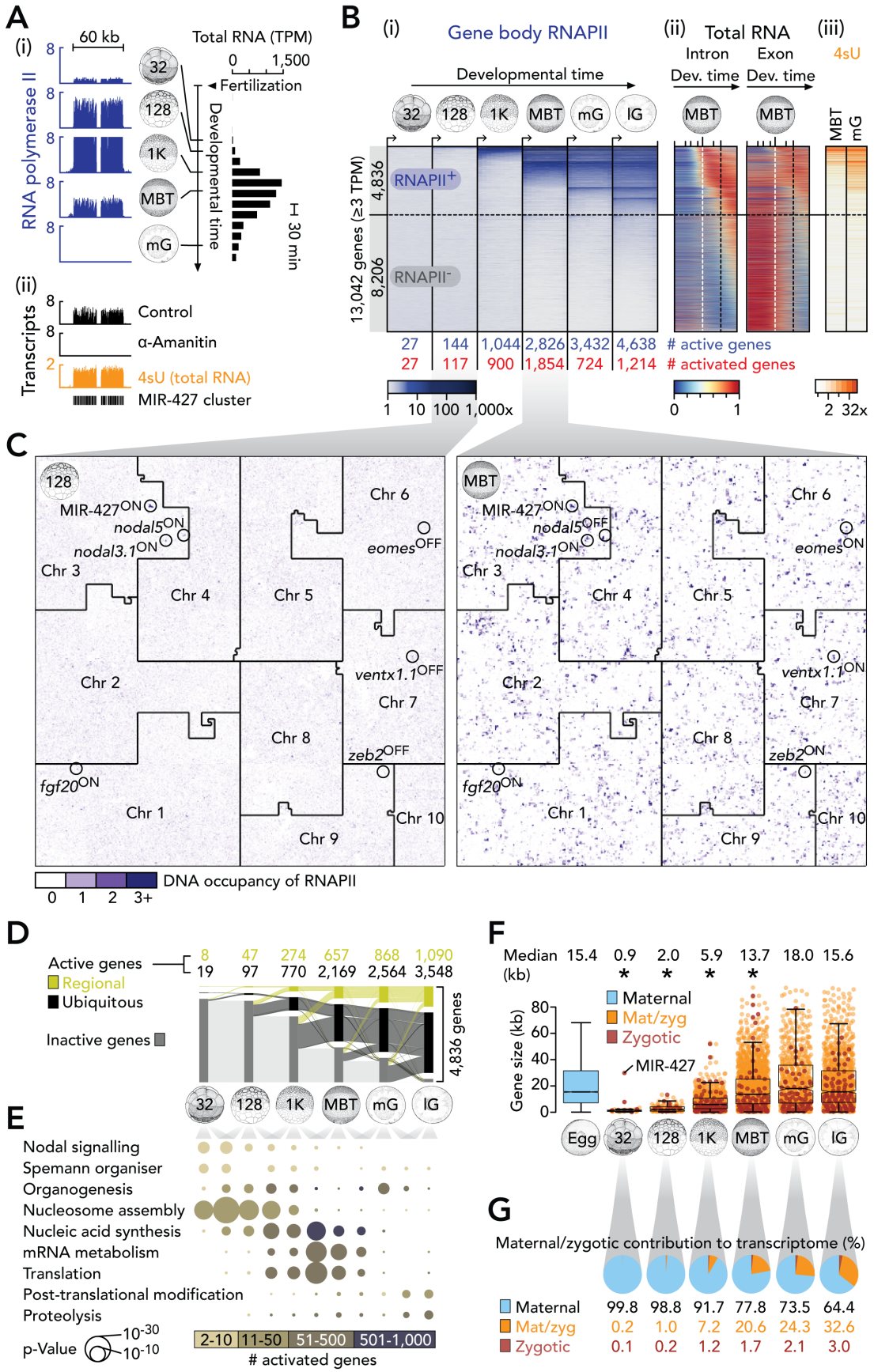

611

612 **Figure 1. Dynamics and Architecture of ZGA in *X. tropicalis***

613 (A) (i) Genome-wide profiling of RNAPII and total RNA (Owens et al., 2016) to determine
614 temporal ZGA dynamics. (ii) Complementary approach to detect transcriptionally active genes
615 by α-amanitin-induced loss and 4sU-enrichment of nascent (zygotic) transcripts.
616 (B) Progression of ZGA from the 32-cell to the late gastrula stage based on (i) whole gene body
617 (full-length) occupancy of RNAPII (i.e., RNAPII was enriched across entire gene bodies; see
618 Transparent Methods). Co-aligned: (ii) High time-resolution of total RNA, separated by intron-
619 and exon-derived signals, from fertilization to the late gastrula stage, and (iii) enrichments of
620 4sU-tagged RNA at the MBT and the mid-gastrula stage. Numbers below RNAPII heat map
621 represent counts of active (blue) and activated (red) genes at the indicated developmental
622 stages. The horizontal dotted line separates RNAPII-engaged ($RNAPII^{+}$) from non-engaged
623 ($RNAPII^{-}$) genes as detected until the late gastrula stage. The vertical dotted lines in the total
624 RNA plots indicate the developmental time points of the MBT (white) and the late gastrula stage
625 (black), respectively.
626 (C) 2D space-filling (Hilbert) curves showing RNAPII recruitment to chromosomes (Chr) at the
627 128-cell stage and the MBT. A few zygotic genes are highlighted as being active (ON) or not
628 (OFF) based on their engagement with RNAPII.
629 (D) Alluvial diagram of spatio-temporal ZGA. Tissue-specificity inferred from regional transcript
630 enrichments along the animal-vegetal or the dorso-ventral axes or both (Blitz et al., 2017).
631 (E) ZGA-associated enrichment of biological processes.
632 (F) Length of maternal and/or zygotic genes. *, $p < 1.9e-7$ (Wilcoxon rank-sum test against
633 maternal and post-MBT activated genes); r_{effect} 0.06 ('MBT' vs 'Egg') - 0.48 ('128' vs 'mG').
634 (G) Maternal/zygotic contribution to the transcriptome deduced from full-length RNAPII
635 occupancy and maternally inherited RNA.
636 Abbreviations: 32, 32-cell; 128, 128-cell; 1K, 1,024-cell; MBT, mid-blastula transition; mG, mid-
637 gastrula; lG, late gastrula; 4sU, 4-thiouridine; Mdn, median; TPM, transcripts per million.
638 See also Figure S1 and Tables S1 and S2.

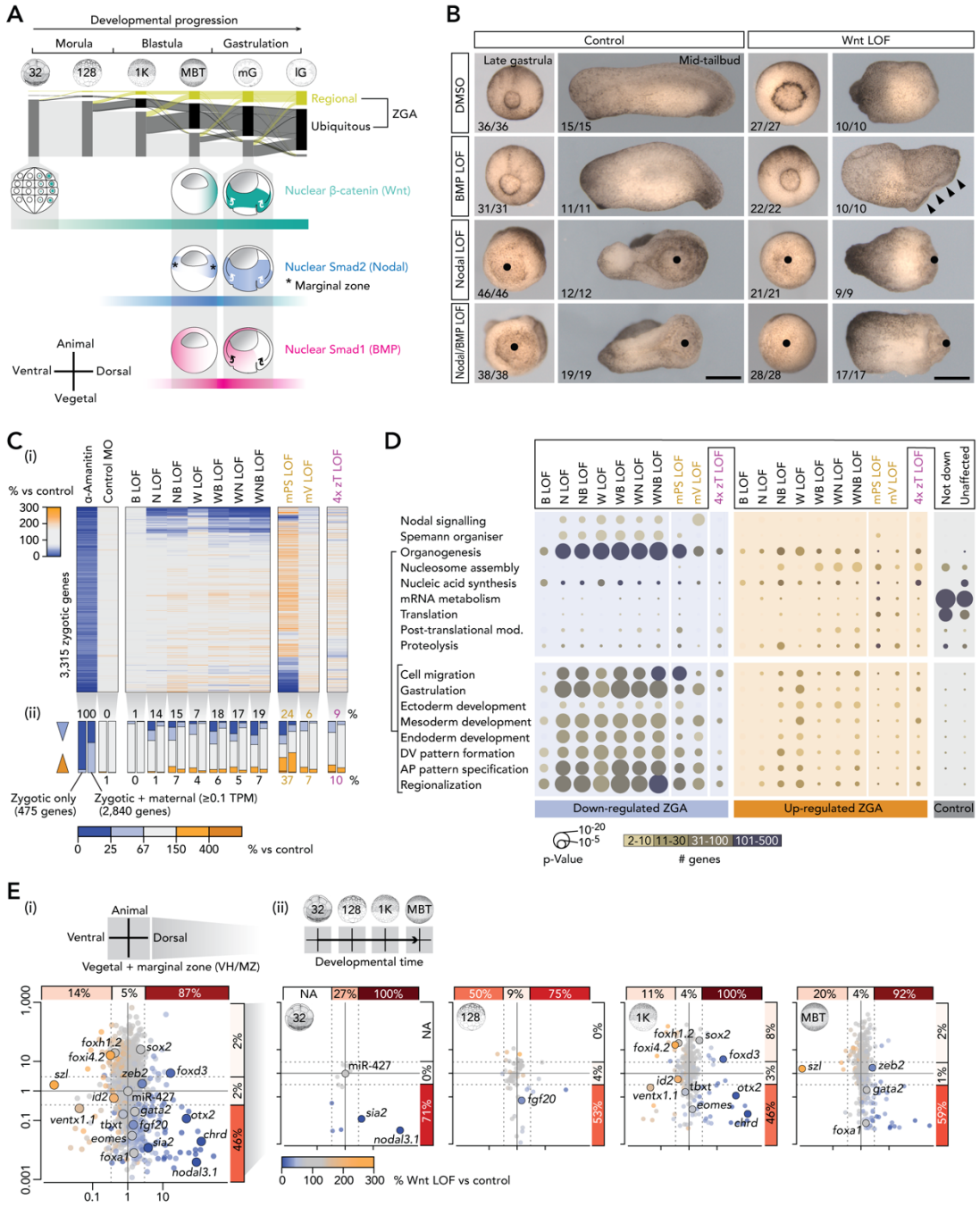

Figure 2. Spatio-temporal ZGA Regulated by Canonical Wnt, Nodal and BMP Signals

(A) Spatio-temporal ZGA and nuclear localization of signal mediators β-catenin (canonical Wnt), Smad2 (Nodal) and Smad1 (BMP) (Faure et al., 2000; Larabell et al., 1997; Schohl and Fagotto, 2002) from the 32-cell to the late gastrula stage.

(B) Morphological phenotypes of single and combined signal LOFs at the late gastrula and the mid-tailbud stage. Left ('control') pictures are taken from Gentsch et al. (2018b). Bullet points, failed blastopore formation. Arrowheads, excessive neural fold formation. Scale bar, 0.5 mm.

(C) Heat map (i) and bar graph summary (ii) of ZGA mis-regulated in various LOF embryos: α-amanitin, positive control; control MO, negative control. Abbreviations: B, BMP; N, Nodal; W, canonical Wnt; mPS, maternal Pou5f3/Sox3; mV, maternal VegT; 4x zT, four zygotic T-box TFs (zygotic VegT, Eomes, Tbxt and Tbxt.2).

(D) Biological processes enriched with mis-regulated and control (not down-regulated or unaffected by the loss of maternal TFs or signaling) sets of zygotic genes under indicated LOFs.
(E) Summary (i) and temporal resolution (ii) of Wnt LOF effects on regional ZGA. Percentages only refer to the down-regulated genes among all zygotic genes with similar expression ratios along the animal-vegetal or the dorso-ventral axes.
See also Figure S2, Tables S1 and S3, and Movie S1.

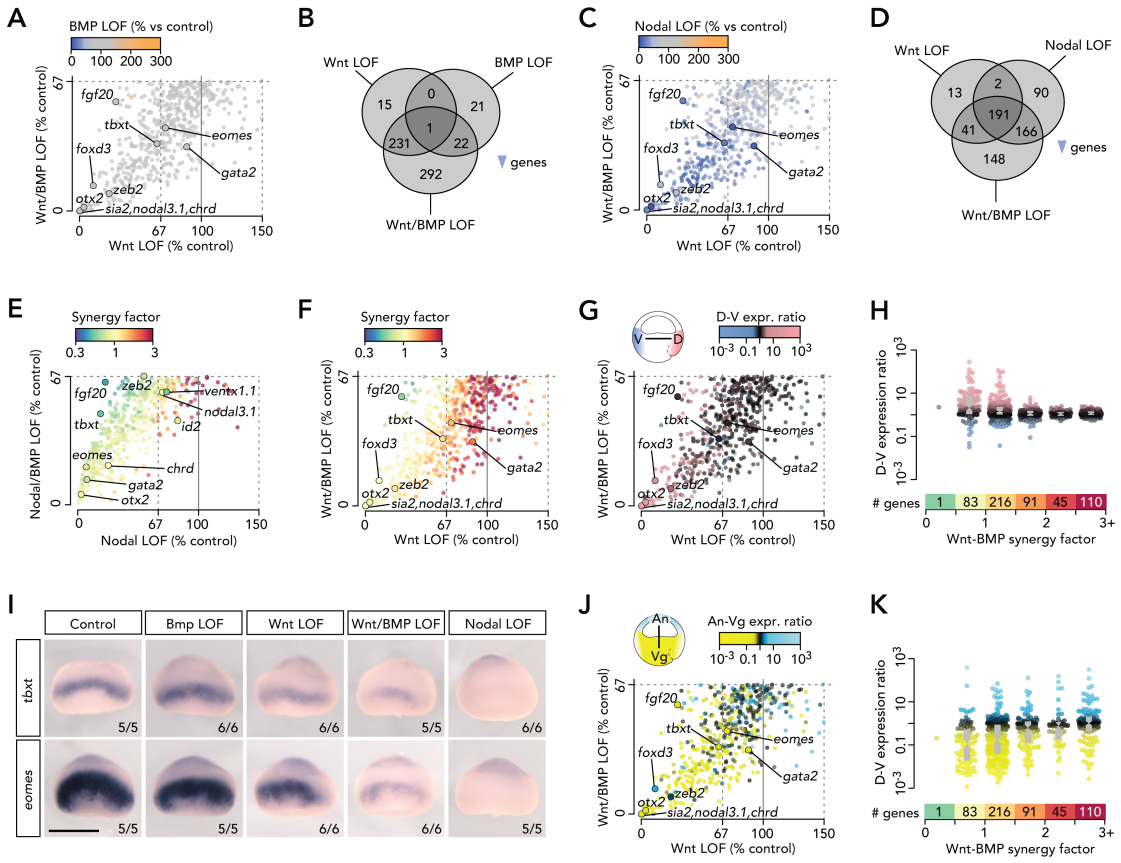

Figure 3. Uniform Gene Expression Across Dorso-Ventral Axis Achieved by Wnt/BMP Synergy.

(A,C,E,F,G,J) Scatter plots of relative (% to control) transcript levels between indicated LOFs with each dot (gene) color-coded according to a third attribute: (A,B) relative (% to control) transcript levels, (E,F) synergy factors between single inductive signals, and (G,J) regional expression ratios between opposite ends of the indicated axis.
(B,D) Venn diagram of down-regulated genes by indicated LOFs.
(H,K) Box and beeswarm plots of regional expression (as measured along the indicated axes) depending on increased Wnt-BMP synergy.
(I) WMISH of *tbxt* and *eomes* transcripts under various LOFs. Control and Nodal LOF pictures are from Gentsch et al. (2018b).
See also Figure S3 and Table S3.

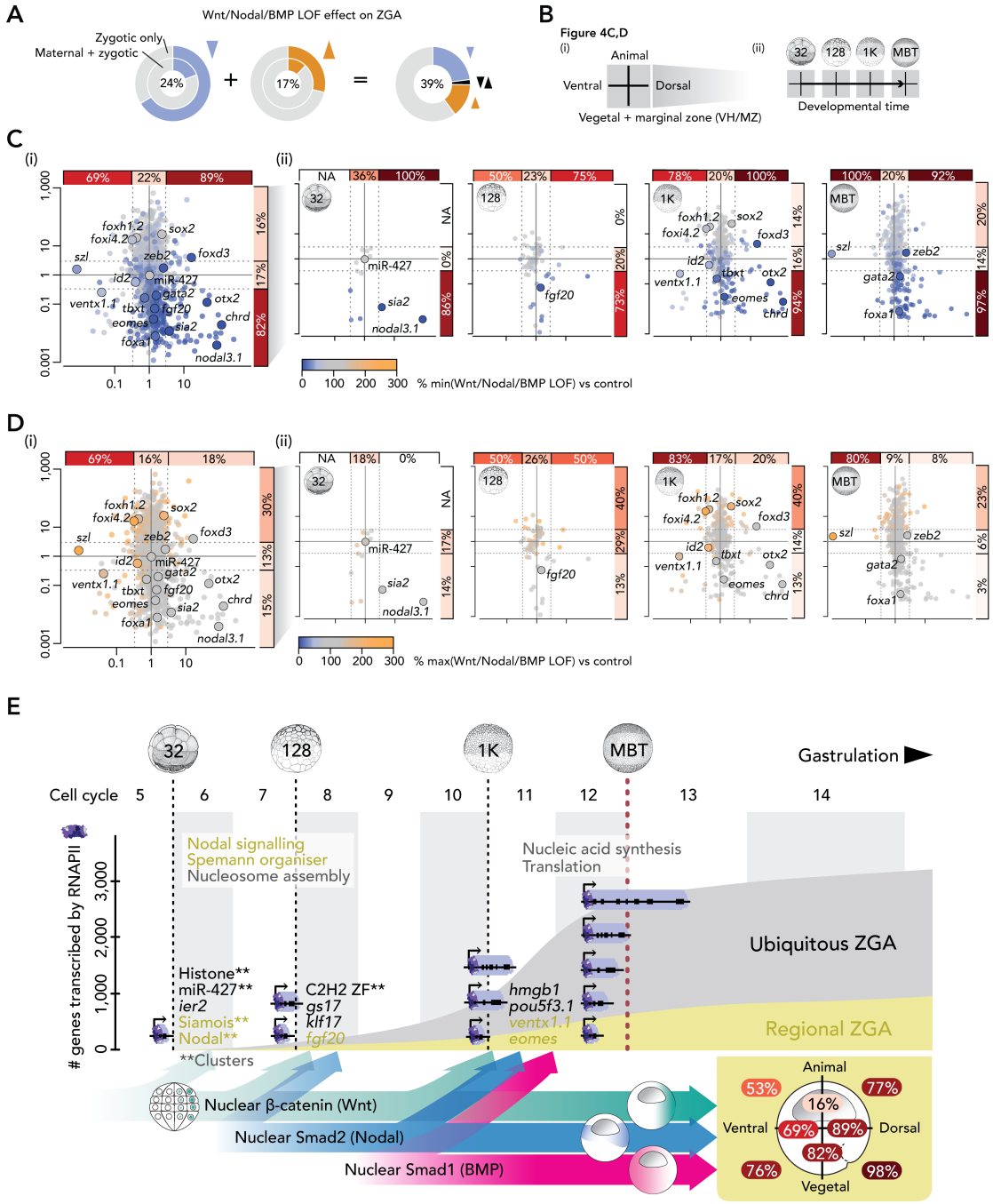

Figure 4. Canonical Wnt, Nodal and BMP Signals Induce the Majority of Regional ZGA.

(A) Total percentage of active (zygotic only and maternal-zygotic) genes mis-regulated by Wnt, Nodal and/or BMP LOF.

(B) Graphical explanations of figure panels (C) and (D).

(C,D) Summary (i) and temporal resolution (ii) of minimal (C) and maximal (D) transcript levels of active genes (separated by regional expression along the primary body axes) detected among Wnt, Nodal and/or BMP LOFs. Percentages only refer to the down-regulated (C) or up-regulated (D) genes among all zygotic genes with the same range of expression ratios along the animal-vegetal or dorso-ventral axes.

(E) Exponential activation of gradually longer genes before the MBT (bulk ZGA) when cell divisions occur at rapid and nearly constant intervals (~20 min at 28ºC). Sequential induction

682 of the canonical Wnt, Nodal and BMP pathway is critical to high percentages of regional ZGA
683 (as measured along the two primary body axes within the indicated halves and quadrants of an
684 early gastrula embryo): e.g. ~89% or ~98% of gene expression enriched in the dorsal half or
685 vegetal-dorsal quadrant, respectively.

686 **SUPPLEMENTAL INFORMATION**

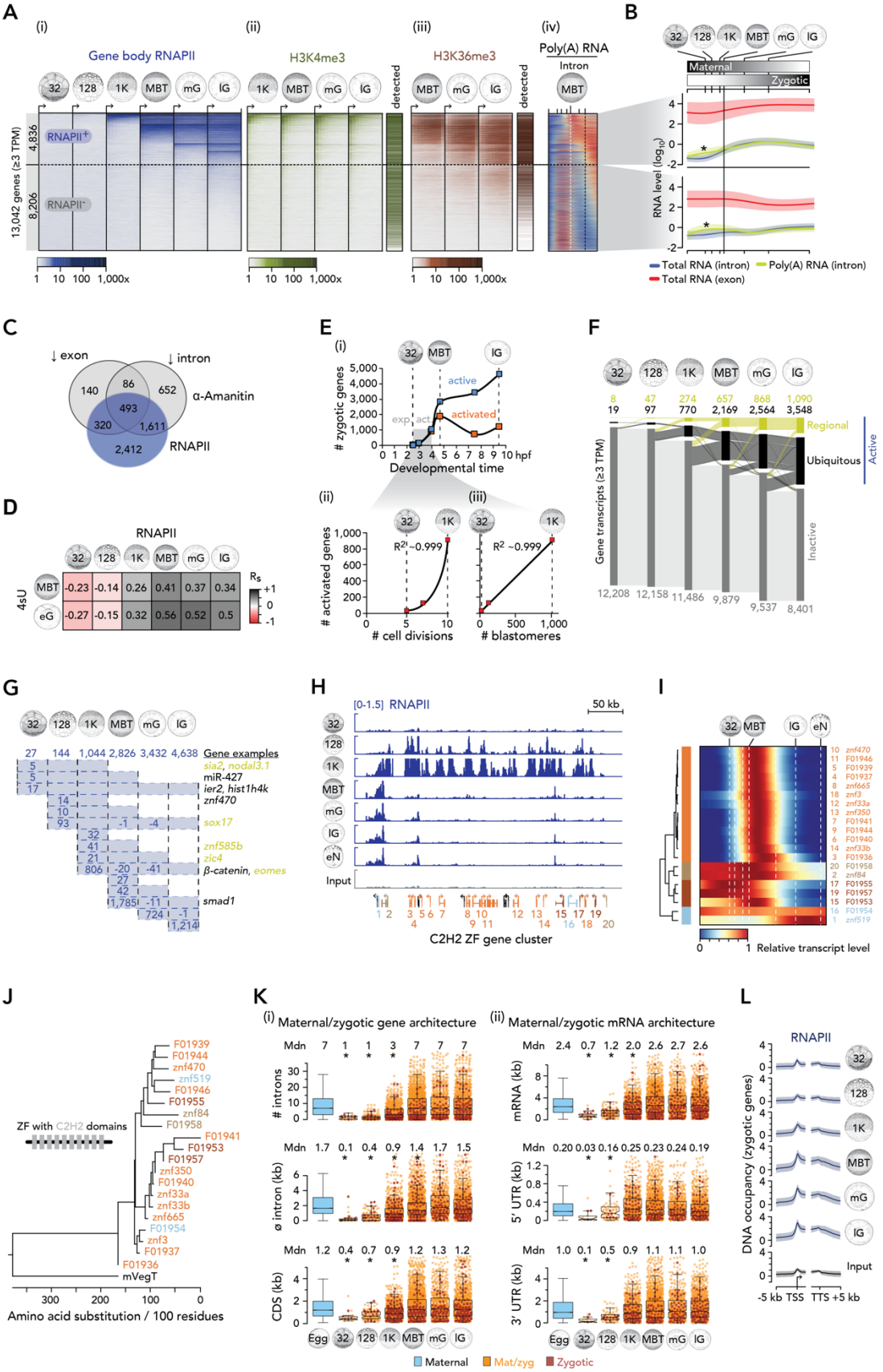

687

688 **Figure S1. Dynamics and Architecture of ZGA in *X. tropicalis*, Related to Figure 1.**

689 (A) Progression of ZGA from the 32-cell to the late gastrula stage based on (i) whole gene body
690 (full-length) occupancy of RNAPII (i.e., RNAPII was enriched across entire gene bodies; see
691 Transparent Methods). Co-aligned: Active histone marks H3K4me1 (ii) and H3K36me3 (iii)
692 (Hontelez et al., 2015) and intronic signal from the high time-resolution profile of poly(A) RNA
693 (iv) (Owens et al., 2016). The horizontal dotted line separates RNAPII-engaged ($RNAPII^+$) from
694 non-engaged ($RNAPII^-$) genes as detected until the late gastrula stage. The vertical dotted lines
695 in the poly(A) RNA plot indicate the developmental time points of the MBT (white) and the late
696 gastrula stage (black), respectively.
697 (B) Transcript feature levels (mean +/- SD) during the maternal-to-zygotic transition. Asterisk,
698 polyadenylation immediately after fertilization (Collart et al., 2014) transiently increased the
699 intronic signal obtained from the poly(A) RNA samples.
700 (C) Venn diagram of zygotic genes detected by full-length RNAPII occupancy or reduced exonic
701 or intronic transcript counts upon blocking RNAPII-mediated transcription with α-amanitin.
702 (D) Pairwise Spearman's correlations (R_s) of enrichment values resulting from RNAPII profiling
703 and 4sU tagging to detect zygotic genes at indicated developmental stages.
704 (E) Plots of the number of active and newly activated genes (i) or newly activated genes versus
705 the developmental time (i), the number of completed cell divisions (ii) or formed blastomeres
706 (iii).
707 (F) Alluvial diagram of spatio-temporal ZGA including maternally inherited RNA transcripts of
708 genes not activated by the late gastrula stage. Tissue-specificity inferred from regional
709 transcript enrichments along the animal-vegetal or the dorso-ventral or both axes (Blitz et al.,
710 2017).
711 (G) Numbers of genes with full-length RNAPII occupancy at indicated developmental stages.
712 Examples of ubiquitously (black) and tissue-specifically (orange) expressed genes are listed to
713 the right.
714 (H) RNAPII dynamics at the Cys2-His2 [C2H2] zinc finger (ZF) cluster from the 32-cell to the
715 early neurula stage.
716 (I) Expression dynamics of C2H2 ZF genes normalized to maximal transcript levels recorded
717 between fertilization and 23.5 hpf (Owens et al., 2016).
718 (J) Phylogenetic tree of the C2H2 ZF genes shown in (H,I). Maternal VegT (mVegT), outgroup
719 TF of this phylogenetic tree.
720 (K) Box and beeswarm plots showing various metrics of the zygotic/maternal genes (i) and
721 mRNA (ii) during ZGA. Asterisks, significant Wilcoxon rank-sum tests against maternal and
722 post-MBT activated genes and corresponding effect sizes (r_{effect}): # introns, $p < 2.1e-13$, r_{effect}
723 0.07-0.43; Ø intron (kb), $p < 7.9e-7$, r_{effect} 0.07-0.42; CDS (kb), $p < 3e-7$, r_{effect} 0.05-0.27; mRNA
724 (kb), $p < 7e-11$, r_{effect} 0.06-0.32; 5' UTR (kb), $p < 0.015$, r_{effect} 0.03-0.15; and 3' UTR (kb), $p < 1.4e-$
725 6, r_{effect} 0.04-0.21.
726 (L) Meta-profiles (mean +/- SD) of RNAPII (separated by developmental stage) and input
727 (negative control) densities at zygotic genes.

728 Abbreviations: 32, 32-cell; 128, 128-cell; 1K, 1,024-cell; MBT, mid-blastula transition; mG, mid-
729 gastrula; lG, late gastrula; eN, early neurula; 4sU, 4-thiouridine; Mdn, median; TPM, transcripts
730 per million.

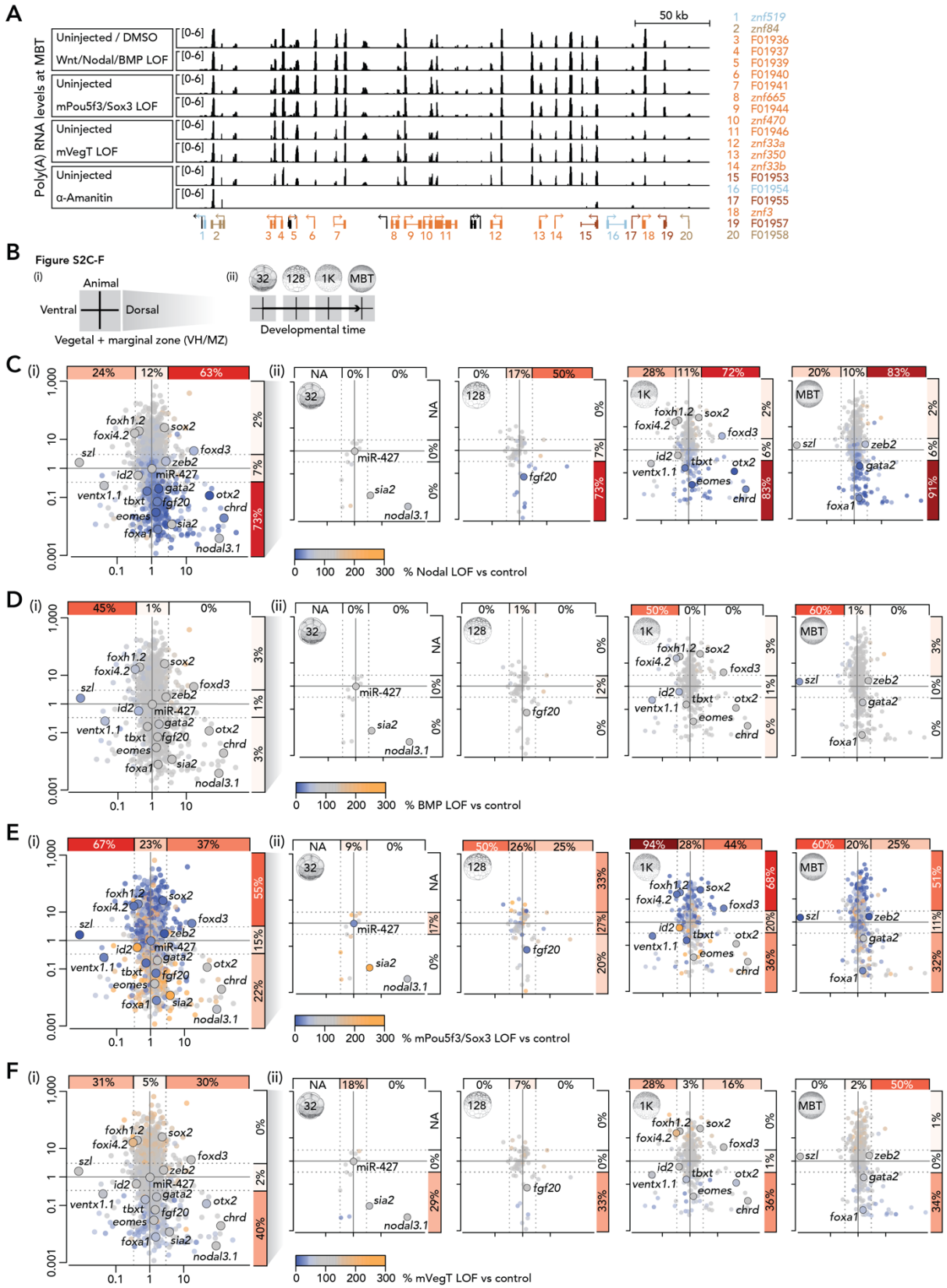

Figure S2. Effect of Canonical Wnt, Nodal and BMP Signals on ZGA, Related to Figure 2.

(A) Poly(A) RNA profiles of the C2H2 ZF cluster (Figure S1H) for indicated control and LOFs at the MBT.

(B) Graphical explanations of figure panels (C-F).

(C-F) Summary (i) and temporal resolution (ii) of gene mis-regulations upon the LOF of Nodal (C) or BMP (D) signaling or maternal Pou5f3/Sox3 (mPou5f3/Sox3) (E) or VegT (mVegT) (F). Percentages only refer to the down-regulated genes (by ≥1/3 compared to control expression level) among all zygotic genes with the same range of expression ratios along the animal-vegetal or the dorso-ventral axes.

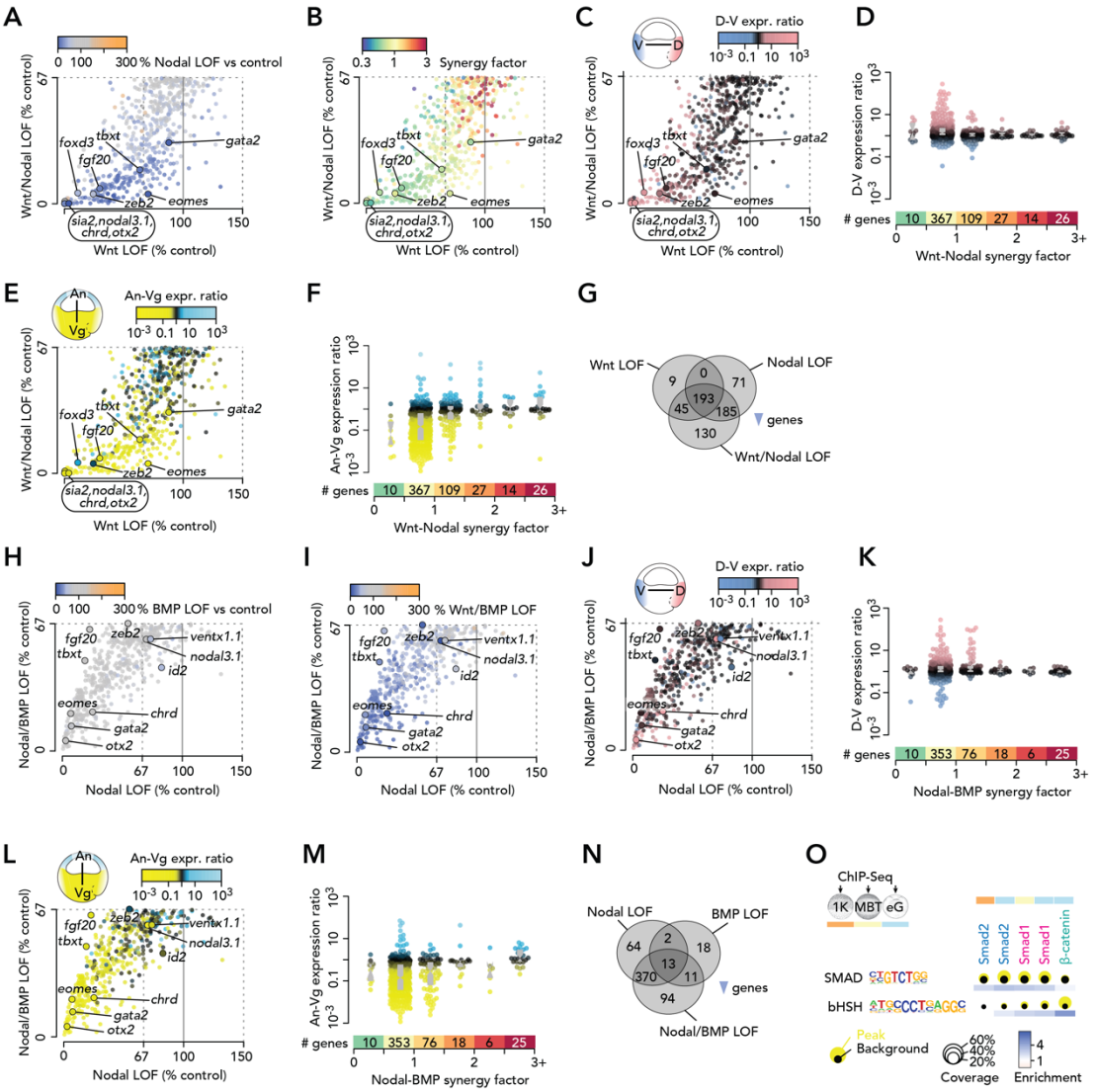

Figure S3. Relationship between Canonical Wnt, Nodal and BMP to Control Regional ZGA, Related to Figure 3.

(A-C,E,H-J,L) Scatter plots of relative (% to control) transcript levels between indicated LOFs with each dot (gene) color-coded according to a third attribute: (A,H,I) relative (% to control) transcript levels, (B) synergy factors between single inductive signals, and (C,E,J,L) regional expression ratios between opposite ends of the indicated axis.

(G,N) Venn diagram of down-regulated genes by indicated LOFs.

(D,F,K,M) Box and beeswarm plots of regional expression (as measured along the indicated axes) depending on increased Wnt-Nodal (D,F) or Nodal-BMP (K,M) synergy.

(O) Coverage and enrichment of Smad and β-catenin-associated DNA motifs (SMAD and

752 bHSH motifs) at endogenous binding sites of β-catenin, Smad1, Smad2 (Gentsch et al., 2018b)
753 at indicated developmental stages (color-coded).

754 **SUPPLEMENTAL TABLES**

755 **Table S1. Summary of Deep sequencing and Read Alignments, Related to Figure 1 and**
756 **2.**
757 The meta-data of ChIP-Seq, 4sU-Seq and RNA-Seq runs includes the developmental stage,
758 condition, read type, and total and genome-aligned read numbers. *, all rows represent
759 manually collected biological sample: a, b and c mark biological replicates. †, library was
760 sequenced twice. Reads were pooled from both sequencing runs. ¶, reported numbers are
761 reads that are non-redundantly aligned to the genome assembly 7.1 with a mapping quality
762 (MAPQ) of 10 (DNA) and 255 (RNA). NF, staging according to Nieuwkoop and Faber (1994).
763 PE/SExx, paired-end or single-end sequencing plus read length.

Sample*	Library	Stage	NF	Condition	PE/SExx	Total reads	Aligned reads¶
1†	RNAPII ChIP	32-cell	6	None	SE50	45,073,468	25,451,597
2†	RNAPII ChIP	128-cell	7	None	SE50/100	65,757,131	41,352,403
3†	RNAPII ChIP	1,024-cell	8	None	SE50	60,445,294	37,661,064
4	RNAPII ChIP	MBT	8.5	None	SE50	29,196,397	18,402,411
5	RNAPII ChIP	mid-gastrula	11	None	SE50	29,268,648	20,085,357
6†	RNAPII ChIP	late gastrula	12+	None	SE50	95,959,570	67,591,256
7	RNAPII ChIP	early neurula	13+	None	SE50	47,039,656	32,889,013
8	4sU-tagged total RNA	Mid-blastula	8+	4sU (4-thiouridine)	PE50	22,202,216	2,738,397
9	4sU-tagged total RNA	Early gastrula	10+	4sU (4-thiouridine)	PE50	20,388,030	5,212,782
10	Total RNA	Mid-blastula	8+	4sU (4-thiouridine), input	PE50	15,087,016	11,451,545
11	Total RNA	Early gastrula	10+	4sU (4-thiouridine), input	PE50	14,902,023	9,771,572
12a	Poly(A)+ RNA	Late blastula	9+	Wnt LOF (β-catenin MO)	PE76	39,439,343	35,540,116
12b	Poly(A)+ RNA	Late blastula	9+	Wnt LOF (β-catenin MO)	PE76	53,523,555	48,364,696
12c	Poly(A)+ RNA	Late blastula	9+	Wnt LOF (β-catenin MO)	PE76	50,568,196	45,534,243
13a	Poly(A)+ RNA	Late blastula	9+	Wnt/Nodal LOF (β-catenin MO, SB431542)	PE76	43,980,513	39,732,439
13b	Poly(A)+ RNA	Late blastula	9+	Wnt/Nodal LOF (β-catenin MO, SB431542)	PE76	44,582,821	40,373,045
13c	Poly(A)+ RNA	Late blastula	9+	Wnt/Nodal LOF (β-catenin MO, SB431542)	PE76	37,243,519	33,648,196
14a	Poly(A)+ RNA	Late blastula	9+	Wnt/BMP LOF (β-catenin MO, LDN193189)	PE76	48,440,801	44,080,313
14b	Poly(A)+ RNA	Late blastula	9+	Wnt/BMP LOF (β-catenin MO, LDN193189)	PE76	40,989,331	37,188,245
14c	Poly(A)+ RNA	Late blastula	9+	Wnt/BMP LOF (β-catenin MO, LDN193189)	PE76	42,494,161	38,527,873
15a	Poly(A)+ RNA	Late blastula	9+	Wnt/Nodal/BMP LOF (β-catenin MO, SB431542, LDN193189)	PE76	52,761,134	47,815,313
15b	Poly(A)+ RNA	Late blastula	9+	Wnt/Nodal/BMP LOF (β-catenin MO, SB431542, LDN193189)	PE76	55,128,794	50,165,817
15c	Poly(A)+ RNA	Late blastula	9+	Wnt/Nodal/BMP LOF (β-catenin MO, SB431542, LDN193189)	PE76	57,414,981	52,101,210
16a	Poly(A)+ RNA	Late blastula	9+	Control (uninjected, DMSO)	PE76	42,248,469	37,989,215
16b	Poly(A)+ RNA	Late blastula	9+	Control (uninjected, DMSO)	PE76	52,066,825	47,105,847
16c	Poly(A)+ RNA	Late blastula	9+	Control (uninjected, DMSO)	PE76	42,875,722	38,893,706

17a	Poly(A)+ RNA	Late blastula	9+	Nodal LOF (SB431542)	PE76	47,946,077	43,367,783
17b	Poly(A)+ RNA	Late blastula	9+	Nodal LOF (SB431542)	PE76	43,201,587	39,270,622
17c	Poly(A)+ RNA	Late blastula	9+	Nodal LOF (SB431542)	PE76	47,497,608	43,105,868
18a	Poly(A)+ RNA	Late blastula	9+	Bmp LOF (LDN193189)	PE76	49,171,585	44,430,698
18b	Poly(A)+ RNA	Late blastula	9+	Bmp LOF (LDN193189)	PE76	35,247,462	31,937,946
18c	Poly(A)+ RNA	Late blastula	9+	Bmp LOF (LDN193189)	PE76	40,645,238	36,899,368
19a	Poly(A)+ RNA	Late blastula	9+	Nodal/BMP LOF (SB431542, LDN193189)	PE76	49,865,847	45,127,683
19b	Poly(A)+ RNA	Late blastula	9+	Nodal/BMP LOF (SB431542, LDN193189)	PE76	48,875,533	44,167,262
19c	Poly(A)+ RNA	Late blastula	9+	Nodal/BMP LOF (SB431542, LDN193189)	PE76	49,397,754	44,710,470
20a	Poly(A)+ RNA	Early gastrula	10+	4x zT (4 zygotic T-box TFs) LOF (zVegT, Eomes, Tbxt, Tbxt.2 MO)	PE76	70,597,621	63,789,737
20b	Poly(A)+ RNA	Early gastrula	10+	4x zT (4 zygotic T-box TFs) LOF (zVegT, Eomes, Tbxt, Tbxt.2 MO)	PE76	62,453,340	56,799,027
20c	Poly(A)+ RNA	Early gastrula	10+	4x zT (4 zygotic T-box TFs) LOF (zVegT, Eomes, Tbxt, Tbxt.2 MO)	PE76	66,378,689	60,011,884
20d	Poly(A)+ RNA	Early gastrula	10+	4x zT (4 zygotic T-box TFs) LOF (zVegT, Eomes, Tbxt, Tbxt.2 MO)	PE76	53,693,870	48,621,416
21a	Poly(A)+ RNA	Mid-gastrula	11+	4x zT (4 zygotic T-box TFs) LOF (zVegT, Eomes, Tbxt, Tbxt.2 MO)	PE76	60,071,724	53,786,168
21b	Poly(A)+ RNA	Mid-gastrula	11+	4x zT (4 zygotic T-box TFs) LOF (zVegT, Eomes, Tbxt, Tbxt.2 MO)	PE76	49,856,218	44,780,174
21c	Poly(A)+ RNA	Mid-gastrula	11+	4x zT (4 zygotic T-box TFs) LOF (zVegT, Eomes, Tbxt, Tbxt.2 MO)	PE76	57,420,101	51,441,091
21d	Poly(A)+ RNA	Mid-gastrula	11+	4x zT (4 zygotic T-box TFs) LOF (zVegT, Eomes, Tbxt, Tbxt.2 MO)	PE76	57,421,959	51,207,446
22a	Poly(A)+ RNA	Late gastrula	12+	4x zT (4 zygotic T-box TFs) LOF (zVegT, Eomes, Tbxt, Tbxt.2 MO)	PE76	59,905,689	53,050,487
22b	Poly(A)+ RNA	Late gastrula	12+	4x zT (4 zygotic T-box TFs) LOF (zVegT, Eomes, Tbxt, Tbxt.2 MO)	PE76	76,564,052	67,801,662
22c	Poly(A)+ RNA	Late gastrula	12+	4x zT (4 zygotic T-box TFs) LOF (zVegT, Eomes, Tbxt, Tbxt.2 MO)	PE76	54,924,184	48,697,757
22d	Poly(A)+ RNA	Late gastrula	12+	4x zT (4 zygotic T-box TFs) LOF (zVegT, Eomes, Tbxt, Tbxt.2 MO)	PE76	56,546,178	49,962,419
23a	Poly(A)+ RNA	Early gastrula	10+	Control (standard control MO)	PE76	57,881,388	52,311,548
23b	Poly(A)+ RNA	Early gastrula	10+	Control (standard control MO)	PE76	49,193,836	44,649,709
23c	Poly(A)+ RNA	Early gastrula	10+	Control (standard control MO)	PE76	78,605,062	70,838,519
23d	Poly(A)+ RNA	Early gastrula	10+	Control (standard control MO)	PE76	67,143,066	60,397,172
24a	Poly(A)+ RNA	Mid-gastrula	11+	Control (standard control MO)	PE76	50,011,338	44,604,698
24b	Poly(A)+ RNA	Mid-gastrula	11+	Control (standard control MO)	PE76	54,847,378	48,981,425
24c	Poly(A)+ RNA	Mid-gastrula	11+	Control (standard control MO)	PE76	56,633,663	50,510,544
24d	Poly(A)+ RNA	Mid-gastrula	11+	Control (standard control MO)	PE76	69,504,876	61,831,845
25a	Poly(A)+ RNA	Late gastrula	12+	Control (standard control MO)	PE76	53,566,350	47,558,871
25b	Poly(A)+ RNA	Late gastrula	12+	Control (standard control MO)	PE76	36,043,121	31,918,744
25c	Poly(A)+ RNA	Late gastrula	12+	Control (standard control MO)	PE76	48,184,154	42,775,598
25d	Poly(A)+ RNA	Late gastrula	12+	Control (standard control MO)	PE76	39,860,708	35,323,477
Total						2,948,234,870	2,524,336,789

764 **Table S2. Temporal Progression of ZGA, Related to Figure 1.**

765 Activated genes are listed according to the earliest developmental stage of full-length RNAPII
766 occupancy. The lists also include the overall enrichment of RNAPII across the gene body, the
767 maternal contribution (TPM) (Owens et al., 2016) and the enrichment of de novo synthesized
768 transcripts determined by 4sU tagging at the MBT and the early gastrula stage.

769 **Table S3. Differential ZGA Analysis, Related to Figure 2, 3 and 4.**

770 Differential expression analysis of genes showing ≥50% (FDR ≤10%) reduced transcript levels
771 in α-amanitin-injected embryos. Normalized transcript levels (inferred from exon or intron
772 counts) are scaled (percentage, %) to the expression level in control embryos. The list also
773 includes FDRs, expression ratios across the animal-vegetal or dorso-ventral axis (Blitz et al.,
774 2017), the earliest developmental stage of full-length RNAPII occupancy, and average
775 expression levels between 0 and 1 hpf (maternal) and 5 and 9 hpf (from the MBT to the mid-
776 gastrula stage).

777 **Movie S1. Quadruple LOF of Zygotic T-box TFs, Related to Figure 2.**
778 Simultaneous filming of the vegetal (top row) and animal (bottom row) hemisphere of 4x zT
779 LOF (labelled as T-box KD in the movie) (left) and control (right) embryos from early gastrula
780 to mid-tailbud stage.

781 TRANSPARENT METHODS

782 CONTACT FOR REAGENTS AND RESOURCE SHARING

783 Further information and requests for resources and reagents should be directed to and will be
784 fulfilled by the Lead Contact, James C. Smith (jim.smith@crick.ac.uk).

785 EXPERIMENTAL MODEL AND SUBJECT DETAILS

786 Xenopus tropicalis Manipulation

787 Standard procedures were used for ovulation, fertilization, and manipulation and incubation of
788 embryos (Khokha et al., 2002; Sive et al., 2000). Briefly, frogs were obtained from Nasco
789 (Wisconsin, USA). Ovulation was induced by injecting serum gonadotropin (Intervet) and
790 chorionic gonadotropin (Intervet) into the dorsal lymph sac of mature female frogs. Eggs were
791 fertilized *in vitro* with sperm solution consisting of 90% Leibovitz's L-15 medium (Thermo Fisher
792 Scientific, Cat#11415064) and 10% fetal bovine serum (Thermo Fisher Scientific,
793 Cat#10500056). After 10 min, fertilized eggs were de-jellied with 2.2% (w/v) L-cysteine (Merck,
794 Cat#168149) equilibrated to pH 8.0. Embryos were cultured in 5% Marc's Modified Ringer's
795 solution (MMR) (5 mM NaCl, 0.1 mM KCl, 0.1 mM $CaCl_2$, 0.05 mM $MgSO_4$ and 0.25 mM HEPES
796 pH7.5) at 21ºC-28ºC. Embryos were staged according to Nieuwkoop and Faber (1994). All
797 *Xenopus* work fully complied with the UK Animals (Scientific Procedures) Act 1986 as
798 implemented by the Francis Crick Institute.

799 Chromatin immunoprecipitation (ChIP)

800 ChIP was carried out as detailed previously (Gentsch and Smith, 2017). Briefly, de-jellied *X.*
801 *tropicalis* embryos were fixed at room temperature with 1% formaldehyde (Merck, Cat#F8775)
802 in 1% MMR for 25 min. The fixation time was extended to 45 min for pre-gastrula stages. The
803 following number of embryos were used for ChIP-Seq: 1,400 at the 32-cell stage, 1,000 at the

804 128-cell stage, 700 at the 1,024-cell stage, 450 at the MBT and 350 for the post-MBT stages.
805 Fixation was terminated by rinsing embryos three times with ice-cold 1% MMR. Fixed embryos
806 were homogenized in CEWB1 (150 mM NaCl, 1 mM EDTA, 1% (v/v) Igepal CA-630 [Merck,
807 Cat#I3021], 0.25% (w/v) sodium deoxycholate [Merck, Cat#SRE0046], 0.1% (w/v) sodium
808 dodecyl sulfate [Merck, Cat#71729] and 10 mM Tris-HCl pH 8.0) supplemented with 0.5 mM
809 DL-Dithiothreitol (Fluorochem, Cat#M02712) and protease inhibitors (Roche,
810 Cat#11873580001). The homogenate was left on ice for 5 min and then centrifuged at 1,000 g
811 (4ºC) for 5 min. Homogenization and centrifugation was repeated once before resuspending
812 the pellet in 1-3 ml CEWB1. Chromatin was solubilized and fragmented by microtip-mediated
813 ultra-sonication (Misonix 3000 sonicator with a tapered 1/16-inch microtip). The solution of
814 fragmented chromatin was cleared by centrifuging at 16,000 g (4ºC) for 5 min. About 1% of the
815 cleared chromatin extract was set aside for the input sample (negative control). The remaining
816 chromatin was incubated overnight at 4ºC on a vertical rotor (10 rpm) with 20 µl of the mouse
817 monoclonal anti-RNAPII (8WG16) (Covance, Cat#MMS-126R; RRID: AB_10013665) antibody.
818 After adding 100 µl of washed protein G magnetic beads (Thermo Fisher Scientific,
819 Cat#10003D) the solution was incubated for another 4 h at 4ºC on a vertical rotor (10 rpm). The
820 beads were washed eight times in CEWB1 and once in TEN (10 mM Tris-HCl pH 8.0, 150 mM
821 NaCl and 1 mM EDTA) at 4ºC. ChIP was eluted off the beads twice with 100 µl SDS elution
822 buffer (50 mM Tris-HCl pH 8.0, 1 mM EDTA and 1% (w/v) sodium dodecyl sulfate) at 65ºC.
823 ChIP eluates were pooled before reversing DNA-protein cross-links. Input (filled up to 200 µl
824 with SDS elution buffer) and ChIP samples were supplemented with 10 µl 5 M NaCl and
825 incubated at 65ºC for 6-16 h. Samples were treated with proteinase K (Thermo Fisher Scientific,
826 Cat#AM2548) and RNase A (Thermo Fisher Scientific, Cat#12091021) to remove any proteins
827 and RNA from the co-immunoprecipitated DNA fragments. The DNA was purified with
828 phenol:chloroform:isoamyl alcohol (25:24:1, pH 7.9) (Thermo Fisher Scientific, Cat#AM9730)
829 using 2.0-ml Phase Lock Gel Heavy microcentrifuge tubes (VWR, Cat#733-2478) for phase
830 separation and precipitated with 1/70 volume of 5 M NaCl, 2 volumes of absolute ethanol and
831 15 µg GlycoBlue (Thermo Fisher Scientific, Cat#AM9516). After centrifugation, the DNA pellet
832 was air-dried and dissolved in 11 µl elution buffer (10 mM Tris-HCl pH 8.5). The DNA
833 concentration was determined on a Qubit fluorometer using high-sensitivity reagents for
834 detecting double-stranded DNA (10 pg/µl to 100 ng/µl) (Thermo Fisher Scientific, Cat#Q33231).
835

836 **ChIP-Seq Library Preparation**

837 Using the KAPA Hyper Prep Kit (Roche, Cat#KK8504), 2.5-5 ng ChIP DNA or 5 ng input DNA were
838 converted into indexed paired-end libraries as previously described (Gentsch and Smith, 2017).
839 Briefly, DNA fragments were end-repaired and A-tailed for 30 min at 20ºC followed by 30 min at
840 65ºC before cooling to 4ºC. 7.5 pmol TruSeq (single index) Y-adapters (IDT) were ligated to the
841 DNA fragment ends for 20 min at 20ºC. The DNA ligation product was extracted with 0.8x SPRI
842 (solid phase reversible immobilisation) beads (Beckman Coulter, Cat#A63882) and amplified in
843 five PCR cycles (15 sec at 98ºC, 30 sec at 60ºC and 30 sec at 72ºC) using the KAPA high-fidelity

844 polymerase master mix (Roche, Cat#KK2602) and 25 pmol Illumina P5 (forward) and P7 (reverse)
845 primers (IDT). After cleaning up the PCR reaction with 1x SPRI beads, the DNA library was size-
846 separated by electrophoresis using E-gel EX agarose gels (Thermo Fisher Scientific,
847 Cat#G401002). A gel slice containing DNA ranging from 250 to 450 bp in size was dissolved
848 shaking in 350 µl QG buffer (Qiagen) using a thermomixer (1,000 rpm) at room temperature. The
849 DNA was purified with MinElute columns (Qiagen, Cat#28604) and eluted off these columns twice
850 using 11 µl elution buffer (10 mM Tris-HCl pH 8.5). The library was re-amplified using another 6-8
851 PCR cycles yielding 100-200 ng DNA without adapter dimer contamination. The DNA library was
852 cleaned up with 1x SPRI beads.
853
854 **Illumina Sequencing**
855 All sequencing libraries were quality controlled: The DNA yield and fragment size distribution were
856 determined by fluorometry and chip-based capillary electrophoresis, respectively. ChIP-Seq and
857 RNA-Seq libraries were sequenced on the Illumina HiSeq 2500 and 4000, respectively, by the
858 Advanced Sequencing Facility of the Francis Crick Institute. Sequencing samples and read
859 alignment results are summarized in Table S1.
860
861 **Post-Sequencing Analysis of ChIP-Seq**
862 Single reads of maximal 50 bases were processed using trim_galore v0.4.2 (Babraham Institute,
863 UK) to trim off low-quality bases (default Phred score of 20, i.e. error probability was 0.01) and
864 adapter contamination from the 3' end. Processed reads were aligned to the *X. tropicalis* genome
865 assembly v7.1 and v9.1 (for Hilbert curves) running Bowtie2 v2.2.9 (Langmead and Salzberg,
866 2012) with default settings (Table S1). Alignments were converted to the HOMER's tag density
867 format (Heinz et al., 2010) with redundant reads being removed (makeTagDirectory -single -tbp 1
868 -unique -mapq 10 -fragLength 175 -totalReads all). Only uniquely aligned reads (i.e. MAPQ ≥10)
869 were processed. We pooled all input alignments from various developmental stages (Gentsch et
870 al., 2018b). This created a comprehensive mappability profile that covered ~400 million unique
871 base pair positions. For Hilbert curves, tag densities were generated across the genome v9.1 using
872 sliding (200-bp increments) 400-bp window. Background signals (<0.3 reads per 1 million mapped
873 reads) were removed. Blacklisted (Gentsch et al., 2018b) regions (except for MIR-427) were
874 excluded using intersectBed (-v -f 0.5) from BEDtools v2.25.0 (Quinlan and Hall, 2010).
875
876 **Detecting Zygotic and Maternal Genes Using RNAPII Profiling and High Time-Resolution**
877 **Transcriptomics**
878 Normalized RNAPII and input tag densities were calculated across the gene body in 10 bins of
879 equal size. Gene annotations v7.1 were altered based on a few known zygotic isoforms and some
880 corrections obtained from assembling total and poly(A) RNA (Owens et al., 2016) from stage 6 to
881 stage 12.5 *de novo* (Pertea et al., 2016). A few genes had previously been annotated as gene
882 clusters due to assembly uncertainties. We reduced the annotation of polycistronic MIR-427 to the
883 minus arm (scaffold_3b:3516900-3523400) and only monitored *nodal3.5* and *nodal5.3* within their

884 respective gene clusters. Gene bodies with <40% mappability were removed. Here, the threshold
885 of mappability per bin was set at 10% of the input read density averaged across all gene bodies in
886 use. Subsequently, enrichment values were only obtained for all mappable bins by dividing read
887 densities of RNAPII and input. Further, we restricted the analysis to genes for which ≥3 transcripts
888 per million (TPM) could be detected on average over three consecutive time points (i.e. over the
889 developmental time of 1 h) of a high-resolution profile of total RNA (Owens et al., 2016) from
890 fertilization to after gastrulation (stage 13). Genes were considered active when RNAPII
891 enrichments along their full length (see thresholds below) and corresponding transcripts (≥0.1
892 TPM) were simultaneously detected. Transcript levels were calculated over three consecutive time
893 points +/- 1 h from the developmental stage of RNAPII profiling. RNAPII enrichment covered ≥80%
894 of the mappable gene body and reached at least one of the following thresholds: (1) 2.6-fold, (2)
895 1.8-fold and 1.4-fold at the next or previous stage, (3) 1.4-fold and 1.8-fold at the next or previous
896 stage, or (4) 1.4-fold over three consecutive stages. The heatmap (Figure 1B and S1A) was sorted
897 by the developmental stage (1st) and the overall fold (2nd) of RNAPII enrichment. Zygotic and
898 maternal contributions to transcriptome (Figure 1G) were based on RNAPII enrichment (see
899 above) and mean transcript levels (≥0.1 TPM) detected between 0 and 1 hpf, respectively.
900
901 **Peak Calling and Motif Enrichment Analysis**
902 Peak calling and motif enrichment analysis were carried out as previously reported (Gentsch et
903 al., 2018b). Briefly, HOMER v4.8.3 (Heinz et al., 2010) was used to identify the binding sites of
904 Smad1 (Gentsch et al., 2018b), Smad2 (Chiu et al., 2014; Gentsch et al., 2018b; Yoon et al., 2011)
905 and β-catenin (Gentsch et al., 2018b; Nakamura et al., 2016) by virtue of ChIP-enriched read
906 alignments (hereafter called peaks): findpeaks -style factor -minDist 175 -fragLength 175 -
907 inputFragLength 175 -fdr 0.001 -gsize 1.435e9 -F 3 -L 1 -C 0.97. This means that both ChIP and
908 input alignments were extended 3' to 175 bp for the detection of significant (FDR ≤0.1%) peaks
909 being separated by ≥175 bp. The effective size of the *X. tropicalis* genome assembly v7.1 was set
910 to 1.435 billion bp, an estimate obtained from the mappability profile (Gentsch et al., 2018b). These
911 peaks showed equal or higher tag density than the surrounding 10 kb, ≥3-fold more tags than the
912 input and ≥0.97 unique tag positions relative to the expected number of tags. To further eliminate
913 any false positive peaks, we removed any peaks with <0.5 CPM and those falling into blacklisted
914 regions showing equivocal mappability due to genome assembly errors, gaps or simple/tandem
915 repeats. Regions of equivocal mappability were identified by a two-fold lower (poor) or three-fold
916 higher (excessive) read coverage than the average detected in 400-bp windows sliding at 200-bp
917 intervals through normalized ChIP input and DNase-digested naked genomic DNA (Gentsch et al.,
918 2018b). All identified regions ≤800 bp apart were subsequently merged. Gap coordinates were
919 obtained from the Francis Crick mirror site of the UCSC genome browser
920 (http://genomes.crick.ac.uk). Simple repeats were masked with RepeatMasker v4.0.6 (Smit et al.)
921 using the crossmatch search engine v1.090518 (Phil Green) and the following settings:
922 RepeatMasker -species "xenopus silurana tropicalis" -s -xsmall. Tandem repeats were masked
923 with Jim Kent's trfBig wrapper script of the Tandem Repeat Finder v4.09 (Benson, 1999) using the

924 following settings: weight for match, 2; weight for mismatch, 7; delta, 7; matching probability, 80;
925 indel probability, 10; minimal alignment score, 50; maximum period size, 2,000; and longest
926 tandem repeat array (-l), 2 [million bp]. The enrichment and occurrence of predetermined DNA
927 binding motifs was calculated using 100 bp centred across the top 2,000 peaks per chromatin
928 feature and developmental stage: findMotifsGenome.pl -size 100 -mknown -nomotif.
929
930 **Injections and Treatments of Embryos**
931 Microinjections were performed using calibrated needles and embryos equilibrated in 4% (w/v)
932 Ficoll PM-400 (Merck, Cat#F4375) in 5% MMR. Microinjection needles were generated from
933 borosilicate glass capillaries (Harvard Apparatus, GC120-15) using the micropipette puller
934 Sutter p97. Maximally three nanolitres were injected into the animal hemisphere of de-jellied
935 zygotes using the microinjector Narishige IM-300. Embryos were transferred to fresh 5% MMR
936 (without Ficoll PM-400) once they reached about the mid-blastula stage.

937 For profiling the nascent transcriptome, embryos were injected with 75 ng 4-thiouridine-5'-
938 triphosphate (4sU) (TriLink BioTechnologies, Cat#N-1025), which is incorporated into newly
939 synthesized transcripts.

940 Loss-of-functions (LOFs) were generated by treating embryos with small molecule inhibitors
941 and/or injecting them with morpholinos (MOs) or α-amanitin. MOs were designed and produced
942 by Gene Tools (Oregon, USA) to block splicing (MO_{splice}) or translation (MO_{transl}): maternal
943 Pou5f3/Sox3 (mPou5f3/Sox3) LOF, 5 ng *Pou5f3.2* MO_{transl} (Chiu et al., 2014; Gentsch et al.,
944 2018b; GCTGTTGGCTGTACATAGTGTC), 5 ng *Pou5f3.3* MO_{transl} (Chiu et al., 2014; Gentsch
945 et al., 2018b; TACATTGGGTGCAGGGACCCTCTCA) and 5 ng *Sox3* MO_{transl} (Gentsch et al.,
946 2018b; GTCTGTGTCCAACATGCTATACATC); maternal VegT (mVegT) LOF, 10 ng m*VegT*
947 MO_{transl} (Gentsch et al., 2018b; Rana et al., 2006; TGTGTTCCTGACAGCAGTTTCTCAT);
948 canonical Wnt LOF, 5 ng *β-catenin* MO_{transl} (Heasman et al., 2000;
949 TTTCAACAGTTTCCAAAGAACCAGG); LOF of four zygotic T-box TFs (4x zT LOF), 2.5 ng *tbxt*
950 *(Xbra, t)* MO_{splice} (Gentsch et al., 2013; TGGAGAGACCCTGATCTTACCTTCC), 2.5 ng *tbxt*
951 *(Xbra, t)* MO_{transl} (Gentsch et al., 2013; GGCTTCCAAGCGCACACACTGGG), 2.5 ng *tbxt.2*
952 *(Xbra3, t2)* MO_{splice} (Gentsch et al., 2013; GAAAGGTCCATATTCTCTTACCTTC), 2.5 ng *tbxt.2*
953 (*Xbra3*, *t2*) MO_{transl} (Gentsch et al., 2013; AGCTGTGCCTGTGCTCATTGTATTG), 5 ng z*VegT*
954 MO_{transl} (Fukuda et al., 2010; Gentsch et al., 2013; CATCCGGCAGAGAGTGCATGTTCCT) and
955 5 ng *eomes* MO_{splice} (Fukuda et al., 2010; Gentsch et al., 2013;
956 GAACATCCTCCTGCAAAGCAAAGAC); control MO, 5-20 ng standard control MO
957 (CCTCTTACCTCAGTTACAATTTATA) according to the dose used for the β-catenin, mVegT
958 and 4x zT LOF experiment; and 30 pg α-amanitin (BioChemica, Cat#A14850001). To block
959 Nodal (Nodal LOF) and BMP (BMP LOF) signaling, embryos were treated with 100 μM
960 SB431542 (Tocris, Cat#1614) and/or 10 μM LDN193189 (Selleckchem, Cat#S2618) from the
961 8-cell stage onwards. Control embryos were treated accordingly with DMSO, in which these
962 antagonists were dissolved. Transcriptional effects of combinatorial signal LOF were

963 determined at late blastula stage (stage 9^+), while those of all other maternal LOFs were
964 determined over three consecutive time points: the MBT (stage 8+), the late blastula (stage 9^+)
965 and the early gastrula (stage 10^+) stage. The 4x zT LOF was transcriptionally profiled at early,
966 mid and late gastrula stage (stage 10^+, 11^+ and 12^+). The 4x zT LOF comparison has four
967 biological replicates (n=4). All other comparisons entail three biological replicates (n=3).

968 **Extraction of Total RNA**

969 Embryos were homogenized in 800 µl TRIzol reagent (Thermo Fisher Scientific,
970 Cat#15596018) by vortexing. The homogenate was either snap-frozen in liquid nitrogen and
971 stored at -80ºC or processed immediately. For phase separation, the homogenate together with
972 0.2x volume of chloroform was transferred to pre-spun 2.0-ml Phase Lock Gel Heavy
973 microcentrifuge tubes (VWR), shaken vigorously for 15 sec, left on the bench for 2 min and
974 spun at ~16,000 g (4ºC) for 5 min. The upper phase was mixed well with one volume of 95-
975 100% ethanol and spun through the columns of the RNA Clean & Concentrator 25 Kit (Zymo
976 Research, Cat#R1017) at ~12,000 g for 30 sec. Next, the manufacturer's instructions were
977 followed for the recovery of total RNA (>17 nt) with minor modifications. First, the flow-through
978 of the first spin was re-applied to the column. Second, the RNA was treated in-column with 3 U
979 Turbo DNase (Thermo Fisher Scientific, Cat#AM2238). Third, the RNA was eluted twice with
980 25 µl molecular-grade water. The concentration was determined on the NanoDrop 1000
981 spectrophotometer or by fluorometry before depleting ribosomal RNA from total RNA (Profiling
982 the Nascent Transcriptome).

983 **Tagging the Nascent Transcriptome**

984 Thirty 4sU-injected embryos were collected at the MBT and the early-to-mid gastrula stage.
985 Total RNA was extracted as outlined above. The 4sU-tagging was performed according to Gay
986 et al. (2014) with few minor modifications. The RNA Clean & Concentrator 5 Kit (Zymo
987 Research, Cat#R1013) was used to purify RNA. Briefly, the Ribo-Zero Gold rRNA Removal Kit
988 (Illumina, Cat#MRZG126) was used according to the manufacturer's instructions to deplete
989 ribosomal RNA from ~10 µg total RNA. The RNA was purified and fragmented for 4 min at 95ºC
990 using the NEBNext Magnesium RNA Fragmentation Module (NEB, Cat#E6150). The RNA was
991 purified again before conjugating HDPD-Biotin (Thermo Fisher Scientific, Cat#21341) to 4sU
992 via disulfide bonds for 3 h in the dark. Purified RNA was mixed with Streptavidin beads (Thermo
993 Fisher Scientific, Cat#65305) to pull down biotin-tagged RNA. The RNA was eluted off the
994 beads by treating them twice with 100 µl pre-heated (80ºC) 100 mM β-mercaptoethanol (Merck,
995 Cat#M6250), which breaks the disulfide bond between Biotin and 4sU. Subsequently, the RNA
996 was converted into a deep sequencing library by following the manual instructions (Rev. C,
997 8/2014) of the ScriptSeq v2 RNA-Seq Library Preparation Kit (Illumina, Cat#SSV21106) starting
998 with 4.1.A. (Anneal the cDNA Synthesis Primer) and 4.1.B. (Synthesize cDNA), RNA and
999 ending with part 3.C (Synthesize 3'-Tagged DNA) to 3.G. (Assess Library Quantity and Quality).
1000 cDNA was purified using 1.8x SPRI beads. Input and 4sU-enriched cDNA were PCR-amplified
1001 with 11 and 15 cycles, respectively. The 4sU RNA-Seq library was purified with 1x SPRI beads.

1002 **Post-Sequencing Analysis of 4sU Tagging**
1003 Paired-end reads were aligned to the *X. tropicalis* transcriptome assembly v7.1 running Bowtie2
1004 (Langmead and Salzberg, 2012) with the following constraints: -k 200 (maximal allowed number
1005 of alignments per fragment) -X 800 (maximum fragment length in bp) --rdg 6,5 (penalty for read
1006 gaps of length N, 6+N*5) --rfg 6,5 (penalty for reference gaps of length N, 6+N*5) --score-main
1007 L,-.6,-.4 (minimal alignment score as a linear function of the read length x, f(x) = -0.6 - 0.4*x) -
1008 -no-discordant (no paired-end read alignments breaching maximum fragment length X) --no-
1009 mixed (only concordant alignment of paired-end reads). Only read pairs that uniquely align to
1010 one gene were counted. Raw read counts were normalized with DESeq2 v1.22.1 (Love et al.,
1011 2014) and then scaled to the input.

1012 **Poly(A) RNA-Seq Profiling**
1013 10-15 embryos were collected per stage and condition. Total RNA was extracted as outlined
1014 above. Libraries were made from ~1 µg total RNA by following the low-sample protocol of the
1015 TruSeq RNA Library Prep Kit v2 (Illumina, Cat#RS-122-2001) with a few modifications. First, 1 µl
1016 cDNA purified after second strand synthesis was quantified on a Qubit fluorometer using high-
1017 sensitivity reagents for detecting double-stranded DNA (10 pg/µl to 100 ng/µl). By this stage, the
1018 yield was ~10 ng. Second, the number of PCR cycles was reduced to eight to avoid products of
1019 over-amplification such as chimera fragments.
1020
1021 **Poly(A) RNA-Seq Read Alignment**
1022 Paired-end reads were aligned to the *X. tropicalis* genome assembly v7.1 using STAR v2.5.3a
1023 (Dobin et al., 2013) with default settings. The alignment was guided by a revised version of the
1024 gene models v7.2 (Collart et al., 2014) to improve mapping accuracy across splice junctions. The
1025 alignments were sorted by read name using the sort function of Samtools v1.3.1 (Li et al., 2009).
1026 Exon and intron counts (-t 'exon;intron') were extracted from unstranded (-s 0) alignment files using
1027 VERSE v0.1.5 (Zhu et al., 2016) in featureCounts (default) mode (-z 0). Intron coordinates were
1028 adjusted to exclude any overlap with exon annotation. For visualization, genomic BAM files of
1029 biological replicates were merged using Samtools and converted to the bigWig format. These
1030 genome tracks were normalized to the wigsum of 1 billion excluding any reads with mapping quality
1031 <10 using the python script bam2wig.py from RSeQC v2.6.4 (Wang et al., 2012).
1032
1033 **Differential Gene Expression Analysis**
1034 Differential expression analysis was performed with both raw exon and intron counts excluding
1035 those belonging to ribosomal and mitochondrial RNA using the Bioconductor/R package
1036 DESeq2 v1.22.1 (Love et al., 2014). In an effort to find genes with consistent fold changes over
1037 time, p-values were generated according to a likelihood ratio test reflecting the probability of
1038 rejecting the reduced (~ developmental stage) over the full (~ developmental stage + condition)
1039 model. Resulting p-values were adjusted to obtain false discovery rates (FDR) according to the
1040 Benjamini-Hochburg procedure with thresholds on Cook's distances and independent filtering
1041 being switched off. Equally, combinatorial LOF profiling and regional expression datasets (Blitz

1042 et al., 2017) without time series were subjected to likelihood ratio tests with reduced (~ 1) and
1043 full (~ condition) models for statistical analysis. Fold changes of intronic and exonic transcript
1044 levels were calculated for each developmental stage and condition using the mean of DESeq2-
1045 normalized read counts from biological replicates. Both intronic and exonic datasets were
1046 filtered for ≥10 DESeq2-normalized read counts that were detected at least at one
1047 developmental stage in all uninjected or DMSO-treated samples. Gene-specific fold changes
1048 were removed at developmental stages that yielded <10 normalized read counts in
1049 corresponding control samples. Next, the means of intronic and exonic fold changes were
1050 calculated across developmental stages. The whole dataset was confined to 3,318 genes for
1051 which at least 50% reductions (FDR ≤10%) in exonic (default) or intronic counts could be
1052 detected in α-amanitin-injected embryos. Regional expression was based on exonic read
1053 counts by default unless the intronic fold changes were significantly (FDR ≤10%) larger than
1054 the exonic fold changes (Table S3). For the hierarchical clustering of relative gene expression
1055 (Figure 2C), increased transcript levels were masked and only data points from signal LOFs,
1056 mPou5f3/Sox3 LOF and 4x zT LOF embryos were used. Euclidean distance-derived clusters
1057 were linked according to Ward's criterion and sorted using the optimal leaf ordering (OLO)
1058 algorithm. The synergy factor (SF) between signals x and y (Figures 3 and S3) were calculated
1059 as follows: $SF_{xy} = \Delta_{xy} / (\Delta_x + \Delta_y)$. Δ is the relative loss of gene expression caused by signal
1060 depletion. For these calculations, any gene upregulations were neutralised (i.e. set to 1).

1061 **Analysis of Enriched Gene Ontology (GO) Terms**

1062 Over-represented GO terms were found by applying hypergeometric tests of the
1063 Bioconductor/R package GOstats v2.42.0 (Falcon and Gentleman, 2007) on gene lists. The
1064 process was also supported by the Bioconductor/R packages GSEABase v1.44.0 (Morgan et
1065 al., 2017) and GO.db v3.4.1 (Carlson et al., 2007). The gene universe was associated with GO
1066 terms by means of BLAST2GO (Conesa et al., 2005) as previously outlined (Collart et al., 2014;
1067 Gentsch et al., 2015).

1068 **Generation of Hybridization Probes**

1069 Plasmids *X. laevis eomes* pCRII-TOPO (Gentsch et al., 2013) and *X. laevis tbxt (Xbra, t)* pSP73
1070 (Smith et al., 1991) were linearized by restriction digestion (*Bam*HI and *Bgl*II, respectively) and
1071 purified using the QIAquick PCR Purification Kit (Qiagen, Cat#28104). The hybridization probes
1072 were transcribed from ~1 µg linearized plasmid using 1x digoxigenin-11-UTP (Roche,
1073 Cat#11277065910), 40 U RiboLock RNase inhibitor (Thermo Fisher Scientific, Cat#EO0381), 1x
1074 transcription buffer (Roche) and T7 RNA polymerase (Roche, Cat#10881767001) at 37ºC for 2 h.
1075 The probe was treated with 2 U Turbo DNase (Thermo Fisher Scientific) to remove the DNA
1076 template and purified by LiCl precipitation. RNA was diluted to 10 ng/µl (10x stock) with
1077 hybridization buffer. The hybridization buffer (stored at -20ºC) consists of 50% formamide (Fisher
1078 Scientific, Cat#10052370), 5x saline sodium citrate (SSC), 1x Denhardt's solution (Thermo Fisher
1079 Scientific, Cat#750018), 10 mM EDTA, 1 mg/ml torula RNA (Merck, Cat#R6625), 100 µg/ml

1080 heparin (Merck, Cat#H4784), 0.1% (v/v) Tween-20 (Merck, Cat#P9416) and 0.1% (w/v) CHAPS
1081 (Merck, Cat#C3023).
1082
1083 **Whole-Mount In Situ Hybridization (WMISH)**
1084 WMISH was conducted using digoxigenin-labeled RNA probes (Monsoro-Burq, 2007; Sive et
1085 al., 2000). Briefly, *X. tropicalis* embryos were fixed in MEMFA (100 mM MOPS pH 7.4, 2 mM
1086 EDTA, 1 mM $MgSO_4$ and 3.7% formaldehyde) at room temperature for 1 h. The embryos were
1087 then washed once in 1x PBS and two to three times in ethanol. Fixed and dehydrated embryos
1088 were kept at -20ºC for ≥24 h to ensure proper dehydration before starting hybridization.
1089 Dehydrated embryos were washed once more in ethanol before rehydrating them in two steps
1090 to PBT (1x PBS and 0.1% (v/v) Tween-20). Embryos were treated with 5 µg/ml proteinase K
1091 (Thermo Fisher Scientific) in PBT for 6-8 min, washed briefly in PBT, fixed again in MEMFA for
1092 20 min and washed three times in PBT. Embryos were transferred into baskets, which were
1093 kept in an 8x8 microcentrifuge tube holder sitting inside a 10x10 slot plastic box filled with PBT.
1094 Baskets were built by replacing the round bottom of 2-ml microcentrifuge tubes with a Sefar
1095 Nitex mesh. This container system was used to readily process several batches of embryos at
1096 once. These baskets were maximally loaded with 40 to 50 *X. tropicalis* embryos. The
1097 microcentrifuge tube holder was used to transfer all baskets at once and to submerge embryos
1098 into subsequent buffers of the WMISH protocol. Next, the embryos were incubated in 500 µl
1099 hybridization buffer (see recipe above) for 2 h in a hybridization oven set to 60ºC. After this pre-
1100 hybridization step, the embryos were transferred into 500 µl digoxigenin-labeled probe (1 ng/µl)
1101 preheated to 60ºC and further incubated overnight at 60ºC. The pre-hybridization buffer was
1102 kept at 60ºC. The next day embryos were transferred back into the pre-hybridization buffer and
1103 incubated at 60ºC for 10 min. Subsequently, they were washed three times in 2x SSC/0.1%
1104 Tween-20 at 60ºC for 10 min, twice in 0.2x SSC/0.1% Tween-20 at 60ºC for 20 min and twice
1105 in 1x maleic acid buffer (MAB) at room temperature for 5 min. Next, the embryos were treated
1106 with blocking solution (2% Blocking Reagent [Merck, Cat#11096176001] in 1x MAB) at room
1107 temperature for 30 min, and incubated in antibody solution (10% lamb serum [Thermo Fisher
1108 Scientific, Cat#16070096], 2% Blocking Reagent [Merck], 1x MAB and 1:2,000 Fab fragments
1109 from polyclonal anti-digoxigenin antibodies conjugated to alkaline phosphatase [Roche,
1110 Cat#11093274910; RRID:AB_514497]) at room temperature for 4 h. The embryos were then
1111 washed four times in 1x MAB for 10 min before leaving them in 1x MAB overnight at 4ºC.
1112
1113 On the final day of the WMISH protocol, the embryos were washed another three times in 1x
1114 MAB for 20 min and equilibrated to working conditions of alkaline phosphatase (AP) for a total
1115 of 10 min by submerging embryos twice into AP buffer (50 mM $MgCl_2$, 100 mM NaCl, 100 mM
1116 Tris-HCl pH 9.5 and 1% (v/v) Tween-20). At this stage, the embryos were transferred to 5-ml
1117 glass vials for monitoring the progression of the AP-catalyzed colorimetric reaction. Any
1118 residual AP buffer was discarded before adding 700 µl staining solution (AP buffer, 340 µg/ml
1119 nitro-blue tetrazolium chloride [Roche, Cat#11383213001] and 175 µg/ml 5-bromo-4-chloro-3'-

1120 indolyphosphate [Roche, Cat#11383221001]). The colorimetric reaction was developed at
1121 room temperature in the dark. Once the staining was clear and intense enough, the color
1122 reaction was stopped by two washes in 1x MAB. To stabilize and preserve morphological
1123 features, the embryos were fixed with Bouin's fixative without picric acid (9% formaldehyde and
1124 5% glacial acetic acid [Fisher Scientific, Cat#10171460]) at room temperature for 30 min. Next,
1125 the embryos were washed twice in 70% ethanol/PBT to remove the fixative and residual
1126 chromogens. After rehydration to PBT in two steps, the embryos were treated with weak Curis
1127 solution (1% (v/v) hydrogen peroxide [Merck, Cat#1072090500], 0.5x SSC and 5% formamide)
1128 at 4ºC in the dark overnight. Finally, the embryos were washed twice in PBS before imaging
1129 them in PBS on a thick agarose dish by light microscopy.
1130
1131 **Processing of External Datasets**
1132 High-time (30-min intervals) resolution of total and poly(A) RNA-Seq (GSE65785) was
1133 processed as reported in the original publication (Owens et al., 2016). In addition, intron read
1134 counts were corrected by spike RNA-derived normalization factors. For visualization
1135 normalized exon and intron counts were scaled to the maximal count detected across the time
1136 course and fitted using cubic smoothing splines from 0 to 23.5 hpf: smooth.spline(1:48, x,
1137 spar=0.6). Other RNA-Seq (GSE81458) and ChIP-Seq (GSE67974, GSE30146, GSE53654
1138 and GSE72657) were processed as described in detail above except for H3K4me3 and
1139 H3K36me3 whose enriched regions were detected as follows: findPeaks -style histone -
1140 fragLength 175 -inputFragLength 175 -fdr 0.001 -gsize 1.435e9 -F 2 -C 1 -region -size 350 -
1141 minDist 500. Thus, we detected significant regions of histone modifications (-style histone) of
1142 at least the lengths of two DNA fragments (-size 350) and being separated by at least 500 bp
1143 from each other.
1144
1145 **Generation of Plots and Heatmaps**
1146 Genomic snapshots were generated with the IGV genome browser v2.4-rc6 (Robinson et al.,
1147 2011). All plots and heatmaps were generated using R v3.5.1 (http://cran.r-project.org/). The
1148 following add-on R and Bioconductor packages were used for sorting and graphical
1149 visualization of data: alluvial v0.1-2 (Michał Bojanowsk), beeswarm v0.2.3 (Aron Eklund),
1150 circlize v0.4.5 (Gu et al., 2014), complexHeatmap v1.20.0 (Gu et al., 2016a), dplyr v0.7.8,
1151 ggplot2 v3.1.0 (Wickham, 2016), gplots v3.0.1 (Gregory Warnes and colleagues),
1152 GenomicFeatures v1.34.1 (Lawrence et al., 2013), GenomicRanges v1.38.0 (Lawrence et al.,
1153 2013), HilbertCurve v1.12.0 (Gu et al., 2016b), limma v3.38.2 (Ritchie et al., 2015), rtracklayer
1154 1.42.1 (Lawrence et al., 2009) and seriation v1.2-3 (Hahsler et al., 2008).
1155
1156 **QUANTIFICATION AND STATISTICAL ANALYSIS**
1157 No statistical method was used for determining sample size; rather, we followed the literature
1158 to select the appropriate sample size. The experiments were not randomized. Due to the nature
1159 of experiments, the authors were not blinded to group allocation during data collection and

analysis. Only viable embryos were included in the analysis. Frequencies of shown morphological phenotypes and WMISH patterns are included in every image. The significance of over-represented GO terms was based on hypergeometric tests. Significances of non-normally distributed data points (gene features) across ZGA were calculated using paired Wilcoxon rank-sum tests (alternative hypothesis 'less'). The effect size (r_{effect}) was estimated from the standard normal deviate of the Wilcoxon p-value (p) as previously described (Rosenthal, 1991), r_{effect}=Z/sqrt(N), where Z=qnorm(1-p/2) is the standardized Z-score and N is the number of observations.

For RNA-Seq, biological triplicates were used to account for transcriptional variability between clutches. Each LOF experiment has its own control embryos collected in parallel from the same mothers: exp. #1 (α-amanitin), uninjected embryos; exp. #2 (BMP or Nodal LOF), DMSO-treated embryos; exp. #3 (Wnt LOF), uninjected embryos; exp. #4 (mPou5f3/Sox3 LOF), uninjected embryos; exp. #5 (mVegT LOF), uninjected embryos; exp. #6 (single and combinatorial LOFs of Wnt, Nodal and BMP), DMSO-treated embryos; exp. #7 (combinatorial LOF of 4 zygotic T-box TFs), control MO-injected embryos. The gene expressions of control MO-injected embryos of exp. #2 and #5 were normalized to their corresponding uninjected embryos. The mean of these normalizations and conservative FDR estimations (i.e., higher FDR of the two likelihood ratio tests) were used for the comparison with LOF conditions. RNA-Seq libraries from each experiment were generated simultaneously to mitigate any batch effects. The FDR was controlled for multiple comparisons according to the Benjamini-Hochberg procedure. The exact computational implementation of differential expression analysis is outlined on GitHub (see below).

DATA AND SOFTWARE AVAILABILITY

Sequencing reads (FASTQ files) and raw RNA-Seq read counts reported in this paper are available in the GEO database (www.ncbi.nlm.nih.gov/geo) under the accession numbers GSE113186 and GSE122551. All analyses were performed in R v3.5.1 (Bioconductor v3.8), Perl v5.18.2 (https://www.perl.org) and Python v2.7.12 (http://www.python.org) as detailed above. The R code, genome annotation, intermediate datasets and graphs are available on GitHub at https://github.com/gegentsch/SpatioTemporalControlZGA. Original datasets are also available on Mendeley Data at http://dx.doi.org/10.17632/jn466b4n8v.1.

SUPPLEMENTAL REFERENCES

Benson, G. (1999). Tandem repeats finder: a program to analyze DNA sequences. Nucleic Acids Res. *27*, 573–580.

Blitz, I.L., Paraiso, K.D., Patrushev, I., Chiu, W.T.Y., Cho, K.W.Y., and Gilchrist, M.J. (2017). A catalog of Xenopus tropicalis transcription factors and their regional expression in the early gastrula stage embryo. Dev. Biol. *426*, 409–417.

Carlson, M., Falcon, S., Pages, H., and Li, N. (2007). Bioconductor - GO.db.

1200 Chiu, W.T., Le, R.C., Blitz, I.L., Fish, M.B., Li, Y., Biesinger, J., Xie, X., and Cho, K.W.Y.
1201 (2014). Genome-wide view of TGFβ/Foxh1 regulation of the early mesendoderm program.
1202 Development *141*, 1–114.

1203 Collart, C., Owens, N.D.L., Bhaw-Rosun, L., Cooper, B., De Domenico, E., Patrushev, I.,
1204 Sesay, A.K., Smith, J.N., Smith, J.C., and Gilchrist, M.J. (2014). High-resolution analysis of
1205 gene activity during the Xenopus mid-blastula transition. Development *141*, 1927–1939.

1206 Conesa, A., Götz, S., García-Gómez, J.M., Terol, J., Talón, M., and Robles, M. (2005).
1207 Blast2GO: a universal tool for annotation, visualization and analysis in functional genomics
1208 research. Bioinformatics *21*, 3674–3676.

1209 Dobin, A., Davis, C.A., Schlesinger, F., Drenkow, J., Zaleski, C., Jha, S., Batut, P., Chaisson,
1210 M., and Gingeras, T.R. (2013). STAR: ultrafast universal RNA-seq aligner. Bioinformatics *29*,
1211 15–21.

1212 Falcon, S., and Gentleman, R. (2007). Using GOstats to test gene lists for GO term
1213 association. Bioinformatics *23*, 257–258.

1214 Fukuda, M., Takahashi, S., Haramoto, Y., Onuma, Y., Kim, Y.-J., Yeo, C.-Y., Ishiura, S., and
1215 Asashima, M. (2010). Zygotic VegT is required for Xenopus paraxial mesoderm formation and
1216 is regulated by Nodal signaling and Eomesodermin. Int. J. Dev. Biol. *54*, 81–92.

1217 Gay, L., Karfilis, K.V., Miller, M.R., Doe, C.Q., and Stankunas, K. (2014). Applying thiouracil
1218 tagging to mouse transcriptome analysis. Nat. Protoc. *9*, 410–420.

1219 Gentsch, G.E., and Smith, J.C. (2017). Efficient Preparation of High-Complexity ChIP-Seq
1220 Profiles from Early Xenopus Embryos. Methods Mol. Biol. *1507*, 23–42.

1221 Gentsch, G.E., Owens, N.D.L., Martin, S.R., Piccinelli, P., Faial, T., Trotter, M.W.B., Gilchrist,
1222 M.J., and Smith, J.C. (2013). In vivo T-box transcription factor profiling reveals joint regulation
1223 of embryonic neuromesodermal bipotency. Cell Rep. *4*, 1185–1196.

1224 Gentsch, G.E., Patrushev, I., and Smith, J.C. (2015). Genome-wide snapshot of chromatin
1225 regulators and states in Xenopus embryos by ChIP-Seq. J. Vis. Exp. *96*, e52535.

1226 Gentsch, G.E., Spruce, T., Monteiro, R.S., Owens, N.D.L., Martin, S.R., and Smith, J.C.
1227 (2018a). Innate Immune Response and Off-Target Mis-splicing Are Common Morpholino-
1228 Induced Side Effects in Xenopus. Dev. Cell *44*, 597–610.e10.

1229 Gentsch, G.E., Spruce, T., Owens, N.D.L., and Smith, J.C. (2018b). The role of maternal
1230 pioneer factors in predefining first zygotic responses to inductive signals. bioRxiv 306803.
1231 DOI: https://doi.org/10.1101/306803

1232 Gu, Z. Eils, R., and Schlesner, M. (2016a). Complex heatmaps reveal patterns and
1233 correlations in multidimensional genomic data. Bioinformatics *32*, 2847-2849.

1234 Gu, Z., Eils, R., and Schlesner, M. (2016b). HilbertCurve: an R/Bioconductor package for
1235 high-resolution visualization of genomic data. Bioinformatics *32*, 2372–2374.

1236 Gu, Z., Gu, L., Eils, R., Schlesner, M., and Brors, B. (2014). circlize Implements and
1237 enhances circular visualization in R. Bioinformatics *30*, 2811–2812.

1238 Hahsler, M., Hornik, K., and Buchta, C. (2008). Getting Things in Order: An Introduction to the
1239 R Package seriation. J. Stat. Softw. *25*, 1–34.

1240 Heasman, J., Kofron, M., and Wylie, C. (2000). βCatenin Signaling Activity Dissected in the
1241 Early Xenopus Embryo: A Novel Antisense Approach. Dev. Biol. *222*, 124–134.

1242 Heinz, S., Benner, C., Spann, N., Bertolino, E., Lin, Y.C., Laslo, P., Cheng, J.X., Murre, C.,
1243 Singh, H., and Glass, C.K. (2010). Simple combinations of lineage-determining transcription
1244 factors prime cis-regulatory elements required for macrophage and B cell identities. Mol. Cell
1245 *38*, 576–589.

1246 Hontelez, S., van Kruijsbergen, I., Georgiou, G., van Heeringen, S.J., Bogdanović, O., Lister,
1247 R., and Veenstra, G.J.C. (2015). Embryonic transcription is controlled by maternally defined
1248 chromatin state. Nat. Commun. *6*, 10148.

1249 Khokha, M., Chung, C., Bustamante, E., Gaw, L., Trott, K., Yeh, J., Lim, N., Lin, J., Taverner,
1250 N., Amaya, E., et al. (2002). Techniques and probes for the study of Xenopus tropicalis
1251 development. Dev. Dyn. *225*, 499–510.

1252 Langmead, B., and Salzberg, S.L. (2012). Fast gapped-read alignment with Bowtie 2. Nat.
1253 Methods *9*, 357–359.

1254 Lawrence, M., Gentleman, R., and Carey, V. (2009). rtracklayer: an R package for interfacing
1255 with genome browsers. Bioinformatics *25*, 1841-1842.

1256 Lawrence, M., Huber, W., Pagès, H., Aboyoun, P., Carlson, M., Gentleman, R., Morgan, M.,
1257 and Carey, V. (2013). Software for Computing and Annotating Genomic Ranges. PLoS
1258 Comput. Biol. *9*, e1003118.

1259 Li, H., Handsaker, B., Wysoker, A., Fennell, T., Ruan, J., Homer, N., Marth, G., Abecasis, G.,
1260 Durbin, R., 1000 Genome Project Data Processing Subgroup (2009). The Sequence
1261 Alignment/Map format and SAMtools. Bioinformatics *25*, 2078–2079.

1262 Love, M.I., Huber, W., and Anders, S. (2014). Moderated estimation of fold change and
1263 dispersion for RNA-seq data with DESeq2. Genome Biol. *15*, 550.

1264 Monsoro-Burq, A.H. (2007). A Rapid Protocol for Whole-Mount In Situ Hybridization on
1265 Xenopus Embryos. Cold Spring Harb. Protoc. *2007*, pdb.prot4809.

1266 Morgan, M., Falcon, S., and Gentleman, R. (2017). *GSEABase: Gene set enrichment data*
1267 *structures and methods*.

1268 Nakamura, Y., de Paiva Alves, E., Veenstra, G.J.C., and Hoppler, S. (2016). Tissue- and
1269 stage-specific Wnt target gene expression is controlled subsequent to β-catenin recruitment
1270 to cis-regulatory modules. Development *143*, 1914–1925.

1271 Nieuwkoop, P., and Faber, J. (1994). Normal table of Xenopus laevis (Daudin): a systematical
1272 and chronological survey of the development from the fertilized egg till the end of
1273 metamorphosis. Garland.

1274 Owens, N.D.L., Blitz, I.L., Lane, M.A., Patrushev, I., Overton, J.D., Gilchrist, M.J., Cho,
1275 K.W.Y., and Khokha, M.K. (2016). Measuring Absolute RNA Copy Numbers at High Temporal
1276 Resolution Reveals Transcriptome Kinetics in Development. Cell Rep. *14*, 632–647.

1277 Pertea, M., Kim, D., Pertea, G.M., Leek, J.T., and Salzberg, S.L. (2016). Transcript-level
1278 expression analysis of RNA-seq experiments with HISAT, StringTie and Ballgown. Nat.
1279 Protoc. *11*, 1650–1667.

1280 Quinlan, A.R., and Hall, I.M. (2010). BEDTools: a flexible suite of utilities for comparing
1281 genomic features. Bioinformatics *26*, 841–842.

1282 Rana, A., Collart, C., Gilchrist, M., and Smith, J. (2006). Defining synphenotype groups in
1283 Xenopus tropicalis by use of antisense morpholino oligonucleotides. PLoS Genet. *2*, e193.

1284 Ritchie, M.E., Phipson, B., Wu, D., Hu, Y., Law, C.W., Shi, W., and Smyth, G.K. (2015). limma
1285 powers differential expression analyses for RNA-sequencing and microarray studies. Nucleic

1286 Acids Res. *43*, e47.

1287 Robinson, J.T., Thorvaldsdóttir, H., Winckler, W., Guttman, M., Lander, E.S., Getz, G., and
1288 Mesirov, J.P. (2011). Integrative genomics viewer. Nat. Biotechnol. *29*, 24–26.

1289 Rosenthal, R. (1991). Meta-Analytic Procedures for Social Research. SAGE Publishing.

1290 Sive, H., Grainger, R., and Harland, R. (2000). Early development of Xenopus laevis: A
1291 laboratory manual. Cold Spring Harbor Laboratory Press.

1292 Smit, A., Hubley, R., and Green, P. RepeatMasker Open-4.0. 2013-2015.

1293 Smith, J., Price, B., Green, J., Weigel, D., and Herrmann, B. (1991). Expression of a Xenopus
1294 homolog of Brachyury (T) is an immediate-early response to mesoderm induction. Cell *67*,
1295 79–87.

1296 Wang, L., Wang, S., and Li, W. (2012). RSeQC: quality control of RNA-seq experiments.
1297 Bioinformatics *28*, 2184–2185.

1298 Wickham, H. (2016). ggplot2: Elegant Graphics for Data Analysis. Springer.

1299 Yoon, S.-J., Wills, A.E., Chuong, E., Gupta, R., and Baker, J.C. (2011). HEB and E2A
1300 function as SMAD/FOXH1 cofactors. Genes Dev. *25*, 1654–1661.

1301 Zhu, Q., Fisher, S.A., Shallcross, J., and Kim, J. (2016). VERSE: a versatile and efficient RNA-
1302 Seq read counting tool. bioRxiv 053306. DOI: https://doi.org/10.1101/053306